



Calhoun: The NPS Institutional Archive
DSpace Repository

Theses and Dissertations

1. Thesis and Dissertation Collection, all items

2007-12

ISAR imaging using Fourier and wavelet transforms

Lucrecio, Armando

Monterey, California. Naval Postgraduate School

<http://hdl.handle.net/10945/3109>

Downloaded from NPS Archive: Calhoun



<http://www.nps.edu/library>

Calhoun is the Naval Postgraduate School's public access digital repository for research materials and institutional publications created by the NPS community. Calhoun is named for Professor of Mathematics Guy K. Calhoun, NPS's first appointed -- and published -- scholarly author.

Dudley Knox Library / Naval Postgraduate School
411 Dyer Road / 1 University Circle
Monterey, California USA 93943

NAVAL POSTGRADUATE SCHOOL
Monterey, California



THESIS

ISAR IMAGING USING FOURIER AND
WAVELET TRANSFORMS

by

Armando Jorge Lucrecio

December 2007

Thesis Advisor:
Co-Advisor:

Brett Borden
Roberto Cristi

Approved for public release; distribution is unlimited.

THIS PAGE INTENTIONALLY LEFT BLANK

REPORT DOCUMENTATION PAGE			Form Approved OMB No. 0704-0188
Public reporting burden for this collection of information is estimated to average 1 hour per response, including the time for reviewing instruction, searching existing data sources, gathering and maintaining the data needed, and completing and reviewing the collection of information. Send comments regarding this burden estimate or any other aspect of this collection of information, including suggestions for reducing this burden, to Washington Headquarters Services, Directorate for Information Operations and Reports, 1215 Jefferson Davis Highway, Suite 1204, Arlington, Va 22202-4302, and to the Office of Management and Budget, Paperwork Reduction Project (0704-0188) Washington DC 20503.			
1. AGENCY USE ONLY (Leave blank)	2. REPORT DATE December 2007	3. REPORT TYPE AND DATES COVERED Master's Thesis	
4. TITLE AND SUBTITLE ISAR Imaging Using Fourier and Wavelet Transforms		5. FUNDING NUMBERS	
6. AUTHORS Lucrecio, Armando			
7. PERFORMING ORGANIZATION NAME(S) AND ADDRESS(ES) Naval Postgraduate School Monterey CA 93943-5000		8. PERFORMING ORGANIZATION REPORT NUMBER	
9. SPONSORING/MONITORING AGENCY NAME(S) AND ADDRESS(ES)		10. SPONSORING/MONITORING AGENCY REPORT NUMBER	
11. SUPPLEMENTARY NOTES The views expressed in this thesis are those of the author and do not reflect the official policy or position of the Department of Defense or the U.S. Government.			
12a. DISTRIBUTION/AVAILABILITY STATEMENT Approved for public release; distribution is unlimited.		12b. DISTRIBUTION CODE	
13. ABSTRACT(<i>maximum 200 words</i>) We investigate the ISAR imaging model using two different approaches the Fourier and the wavelet transform. Starting from the weak-scatter far-field model we explain why this approximation it's a Fourier Transform. We investigate the scattering mechanisms from different surfaces. We also analyze and derived the expressions of the scatter from sphere. We briefly discuss the radon transform and why it's not a good approach to our problem. We investigate the results using this time-frequency methods, creating images using synthetic data.			
14. SUBJECT TERMS ISAR, Fourier, Imaging, wavelets scattering		15. NUMBER OF PAGES 81	
		16. PRICE CODE	
17. SECURITY CLASSIFICATION OF REPORT Unclassified	18. SECURITY CLASSIFICATION OF THIS PAGE Unclassified	19. SECURITY CLASSIFICATION OF ABSTRACT Unclassified	20. LIMITATION OF ABSTRACT UU

THIS PAGE INTENTIONALLY LEFT BLANK

Approved for public release; distribution is unlimited

ISAR IMAGING USING FOURIER AND WAVELET TRANSFORMS

Armando Lucrecio
Lieutenant, Portuguese Navy
B. Eng., Naval Academy, Portugal 1999

Submitted in partial fulfillment of the
requirements for the degree of

MASTER OF SCIENCE IN PHYSICS

from the

**NAVAL POSTGRADUATE SCHOOL
December 2007**

Author: Armando Lucrecio

Approved by: Brett Borden
Thesis Advisor

Roberto Cristi
Co-Advisor

James Luscombe
Chairman, Department of Physics

THIS PAGE INTENTIONALLY LEFT BLANK

ABSTRACT

We investigate the ISAR imaging model using two different approaches the Fourier and the wavelet transform. Starting from the weak-scatter far-field model we explain why this approximation it's a Fourier Transform. We investigate the scattering mechanisms from different surfaces. We also analyze and derived the expressions of the scatter from sphere. We briefly discuss the radon transform and why it's not a good approach to our problem. We investigate the results using this time-frequency methods, creating images using synthetic data.

THIS PAGE INTENTIONALLY LEFT BLANK

TABLE OF CONTENTS

I.	INTRODUCTION	1
A.	SYNTHETIC APERTURE RADAR IMAGING	1
II.	THE RADAR SCATTERING MODEL	5
A.	WEAK-SCATTER FAR-FIELD MODEL	5
B.	SCATTERING FROM A SPHERE	7
C.	IMAGING FROM WEAK-SCATTERER FAR-FIELD DATA USING FOURIER ANALYSIS	10
III.	RADON TRANSFORM	15
A.	PRELIMINARY DISCUSSION	15
B.	BACKPROJECTION	17
IV.	TIME-FREQUENCY METHODS	21
A.	ISAR IMAGING USING TIME FREQUENCY TECHNIQUES	21
1.	Short Time Fourier Transform vs. Continuous Wavelet transform	22
B.	EXAMPLE OF A CHIRP USING STFT VS. CWT	26
V.	ISAR IMAGING USING STFT AND CWT	29
A.	BACKHOE DATA DOME	29
1.	Backoe Data Dome Version 1.0	29
B.	ALGORITHM FOR ISAR IMAGING USING TIME-FREQUENCY METHODS	31
C.	TEST CASE 1 : $95^\circ \leq \theta_{AZIMUTH} \leq 102^\circ, \phi_{ELEVATION} = 42^\circ$. .	32
D.	TEST CASE 2 : $38 \leq ELEVATION \leq 42\text{DEG}$ AND $95\text{DEG} \leq$ AZIMUTH $\leq 99\text{DEG}$	36
VI.	CONCLUSIONS	43
	APPENDIX A. MATLAB CODE FOR TEST CASE 1	45
	APPENDIX B. MATLAB CODE FOR TEST CASE 2	53

LIST OF REFERENCES	61
INITIAL DISTRIBUTION LIST	63

LIST OF FIGURES

Figure 1. Spotlight SAR	3
Figure 2. Stripmap SAR	4
Figure 3. Geometry of the radar imaging of a target	5
Figure 4. Scatter mechanism	7
Figure 5. Scatterers	7
Figure 6. Coss-section plot	9
Figure 7. Data space	11
Figure 8. Radar Signals capture method	11
Figure 9. Data interpolation	12
Figure 10. ISAR image	13
Figure 11. Geometry of an HRR profile	15
Figure 12. Backprojection - Image 1	19
Figure 13. Backprojection - Image 2	19
Figure 14. STFT - Application	23
Figure 15. STFT - uncertainty Principle	23
Figure 16. STFT - Basis functions an time/frequency resolution	24
Figure 17. CWT - Basis functions an time/frequency resolution	25
Figure 18. Spectrogram and Scalogram and basis functions and time/frequency resolution of the SFTF and the CWT	25
Figure 19. Division of the frequency domain for the STFT and CWT	26
Figure 20. Chirp's spectrogram	27
Figure 21. Chirp's spectrogram	27
Figure 22. CAD Model of Backhoe Loader	29
Figure 23. Backhoe Data Dome Representation in k-Space	30
Figure 24. ISAR image using STFT with a hamming window with 20 points of size and 50% of overlapping	32

Figure 25. ISAR image using STFT with a hamming window, size 40 points and 50 percent of overlapping	32
Figure 26. ISAR image using STFT with a hamming window size 50 points and 50 percent of overlapping	33
Figure 27. ISAR image using STFT with a hamming window, size 60 points and 50 percent of overlapping	33
Figure 28. ISAR image using STFT with a hamming window, size 80 points and 50 percent of overlapping	34
Figure 29. ISAR image using CWT with a Mexican hat window, using a scale of 1:5	34
Figure 30. ISAR image using CWT with a Mexican hat window, using a scale of 3:6	35
Figure 31. ISAR image using CWT with a Mexican hat window, using a scale of 10:13	35
Figure 32. ISAR image using CWT with a Morlet window, using a scale of 8:16	35
Figure 33. ISAR image using CWT with a Daubechies 2 window	36
Figure 34. ISAR image using STFT with a hamming window size 20 points and 50 percent of overlapping	36
Figure 35. ISAR image using STFT with a hamming window size 40 points and 50 percent of overlapping	37
Figure 36. ISAR image using STFT with a hamming window size 50 points and 50 percent of overlapping	37
Figure 37. ISAR image using STFT with a hamming window size 60 points and 50 percent of overlapping	38
Figure 38. ISAR image using STFT with a hamming window size 80 points and 50 percent of overlapping	38
Figure 39. ISAR image using STFT with a hamming window size 100 points and 50 percent of overlapping	39

Figure 40. ISAR image using CWT with a Mexican hat window, using a scale of 1:5	39
Figure 41. ISAR image using CWT with a Mexican hat window, using a scale of 3:6	40
Figure 42. ISAR image using CWT with a Mexican hat window, using a scale of 10:13	40
Figure 43. ISAR image using CWT with a Morlet window, using a scale of 8:16	40
Figure 44. ISAR image using CWT with a Daubechies 2 window	41
Figure 45. ISAR image using STFT with a hamming window size 40 points and 50 percent of overlapping	41

THIS PAGE INTENTIONALLY LEFT BLANK

LIST OF TABLES

Table I. Military applications of SAR technology	3
--	---

THIS PAGE INTENTIONALLY LEFT BLANK

ACKNOWLEDGMENTS

I wish to thank my wife, Adriana, for her love and encouragement throughout this course, research and study at the NPS and also to my son, Gustavo, who always is an inspiration for me.

I would like to thank my thesis advisor, Professor Brett Borden, for his excellent guidance and knowledge-sharing during my entire thesis research and learning process. I have much to thank him and his many insights that allowed me to make the necessary links through this research. I have been quite touched by his willingness to share and encourage my misgivings and challenges as I made my way through this thesis.

Professor Roberto Cristi has been great in shedding light in digital processing issues. I cannot thank him enough for providing me critical ideas and working with me during the research. I am greatly indebted to him and am thankful for his time and assistance.

I want to thank the professors from the Physics departments that helped me during this time in NPS, specially Professor James Luscombe, Professor Nancy Haegel and Professor Gamani Karusaniri because they were also a great source of inspiration and motivation to me as a NPS student sharing their knowledge during the classes and out of classes, thank you for your time and dedication to the students.

I am thankful to my fellow coursemates, LT Jerry Kim, LT Zachary Cole, Major Soh Wei Ting for their friendship, encouragement and support.

THIS PAGE INTENTIONALLY LEFT BLANK

I. INTRODUCTION

A. SYNTHETIC APERTURE RADAR IMAGING

Radar is an electromagnetic instrument used for detection and localization of targets, such as aircraft, ships and ground vehicles. It transmits energy and receives the backscattered field energy from the target [Ref. 4]. The received signal is then processed to extract information about bearing and distance. The radar as a radio frequency sensor can perform at long ranges with high accuracy independent of weather conditions, in day or night.

With the advent of powerful digital signal processing algorithms, multidimensional signal analysis and inversion in imaging systems may now be formulated via more concrete *theoretical principals*. These principals will be the central topic of this thesis: radar technology and the powerful tools of digital signal processing (DSP) can extract more information from the received signal than just range and bearing. In our case, we want to be able to produce images from moving targets.

The original radar systems measured range to a target (radar scatterer) via time delay, and direction of a target via antenna directivity. In the past, Doppler shifts were used to measure target speed only, until it was discovered that Doppler shifts could be processed to obtain fine resolution in a direction perpendicular to the range or beam direction. Through this latter concept, often credited to Carl Wiley of Goodyear Aerospace in 1951, it was found that two-dimensional images could be made of the targets and of the earth's surface using radar. The method was termed Synthetic Aperture Radar (SAR), referring to the concept of creating the effect of a very long antenna by signal analysis [Ref. 2]. The ability to view or capture a scene improves with a larger aperture (in a binocular or camera), a larger radar antenna aperture, or larger acoustic transducer aperture; the key to *better vision is a larger aperture*. Unfortunately, it is extremely difficult to either build or maintain a *physically* large aperture radar system.

The principal idea behind SAR is to synthesize the effect of a large *physical aperture* radar, whose construction is infeasible. The significance of a *larger aperture* becomes evident in the following example:

The lateral or *cross-range* resolution of a $D = 1$ meter diameter radar antenna with wavelength $\lambda = 1$ meter at the range $R = 1000$ meters is

$$\text{Lateral-resolution} = \frac{R\lambda}{D} = 1000 \text{ meters}, \quad (\text{I.1})$$

which is very poor. Yet, based on the SAR Theory and signal processing, if we move this small 1 meter aperture radar along a *synthetic* aperture with length $D_{eff}=1000$ -meters (D_{eff} stands for *effective* radar diameter or aperture), then the lateral resolution with wavelength $\lambda = 1$ meter at the range $R = 1000$ meters becomes

$$\text{Lateral-resolution} = \frac{R\lambda}{D_{eff}} = 1 \text{ meter}, \quad (\text{I.2})$$

This is a tremendous improvement over the 1000 meter lateral resolution of the small 1 meter physical radar antenna. The aperture of $D_{eff} = 1000$ meters is called a *synthetic aperture* [Ref. 3].

When SAR data are collected by the radar system, the data appear to be quite unfocused. In fact, the received data look much like random noise. As in a hologram, the essential information lies in the phase of the received data, and phase-sensitive processing is needed to obtain a focused image [Ref. 2]. In the 1950s and 1960s, the science of *remote sensing* was developing in the civilian community. From the origins of aerial photography, digital scanners using several optical frequency bands were installed in aircraft and satellites, and people began developing uses for the detailed wide-area images of the Earth's surface that were acquired. Military SAR technology was released to the civilian community in the 1970s, and remote sensing scientists found that SAR images provided a complementary and useful addition to their optical sensors [Ref. 2]. Since synthetic aperture imaging was originally introduced for radar systems, this technology has been used for different military applications shown in table A.

- Automatic Aircraft Landing
- Mine detection
- Concealed target detection in foliage
- Interior imaging of Buildings in a rescue or hostage crisis
- Missile detection and tracking
- Ground moving target detection and tracking
- Airborne Reconnaissance

Table I. Military applications of SAR technology

In this thesis we will focus on - *Airborne Reconnaissance*.

There are two classes of SAR imaging systems: *spotlight SAR*; and *stripmap SAR*. In spotlight SAR the moving radar platform stares at a specific location (usually on the ground) so that at each point in the flight path the same target is illuminated from different directions. The locus of equal range points is determined by the intersection of the radiating spherical wave and the ground. When the ground is assumed to be a plane, these points will form a circle. If the radar antenna beamwidth is narrow and the spot is sufficiently far away, then the data are collected on small arcs that can be approximated as lines. Consequently, the imaging method is mathematically the same as that used in Inverse Synthetic Aperture Radar (ISAR) (see Figure 1)

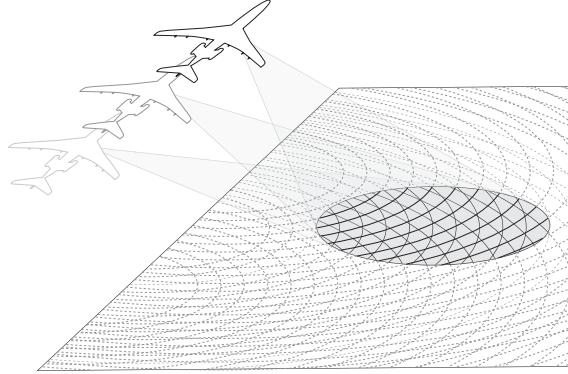


Figure 1. In spotlight SAR the radar is trained on a particular location as the radar platform moves. In this figure the equi-range circles (dotted lines) are formed from the intersection of the radiated spherical wavefront and the surface of a (flat) Earth. This Figure is taken from [Ref. 11]

In contrast, stripmap SAR sweeps the radar beam along with the platform without staring at a particular location on the ground (see Figure 2). The equi-range points are still circles, but the data model based on simple rotation is no longer valid. In fact, since radar doesn't stare at the same location, effective stripmap reconstruction will require *wide* radar beamwidth [Ref. 11].

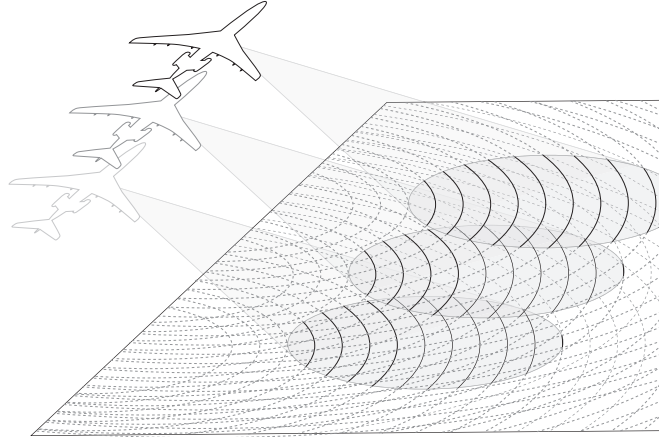


Figure 2. Stripmap SAR acquires data without staring. The radar typically has fixed orientation with respect to the platform and the data are acquired as the beam footprint sweep over the ground. This Figure is taken from [Ref. 11]

In this thesis we will address the construction of ISAR images using two different approaches: Fourier and Wavelet transforms. This thesis will be organized as following: In chapter two we will derive the weak-scatter far-field model. In chapter three we will discuss the Radon transform. In chapter four we will address the difference between the Fourier and the wavelet transforms. In chapter five we will discuss the algorithms and how to construct ISAR images using the two approaches. Finally, in the sixth chapter we will summarize our conclusions.

II. THE RADAR SCATTERING MODEL

A. WEAK-SCATTER FAR-FIELD MODEL

As always we need to start from a mathematical model, to describe what is happening in reality. In our case we are interested in the backscatter field from the target after being illuminated by an electromagnetic wave.

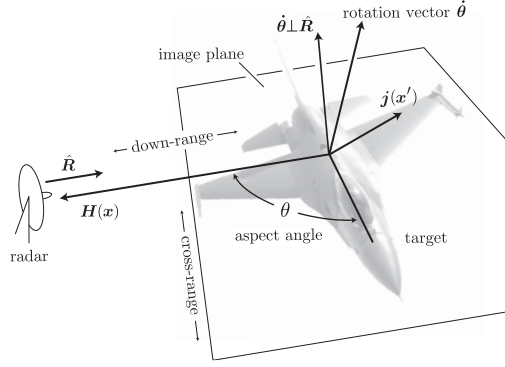


Figure 3. Geometry of the radar imaging of a target. This picture was taken from [Ref. 11]

Let's assume that our incident field is of the form,

$$\mathbf{H}_{inc} = \mathbf{H}_0 e^{i(\mathbf{k}\mathbf{R}\cdot\mathbf{r} - \omega t)} \quad (\text{II.1})$$

where $H = \frac{B}{\mu}$ is the constitutive relation, B is the Magnetic Field, μ is the Magnetic permeability and k is the wave number. If we assume the target to be a perfect conductor (current just on the surface) and that its surface is smooth, then after some algebra we can define the scatter field from a target as follows, [Ref. 11]

$$\mathbf{H}_{scatt}(\mathbf{R}, t : k) = \frac{ik\mathbf{H}_0 e^{i(2k\mathbf{R}\cdot\mathbf{r} - \omega t)}}{(2\pi)^3 R} \int_{\mathbb{V}} \rho_{k, \hat{\mathbf{R}}(x')} e^{i2k\hat{\mathbf{R}}\cdot\mathbf{x}'} dx' dy' dz' \quad (\text{II.2})$$

This is called the weak-scatterer far-field model. The function $\rho_{k, \hat{\mathbf{R}}(x')}$ is defined as a generalized scatterer density function which will generally depend on \mathbf{k} and $\hat{\mathbf{R}}$. It

can be shown that the integrand of equation (II.2) is the far field pattern $F(\theta, \phi)$. This is why (II.2) is called the weak-scatter far-field model. We are interested in this expression because from \mathbf{H}_{scatt} we can extract information about the target of interest by estimating various functions closely related to $\rho_{k, \hat{\mathbf{R}}}$. For our purposes, (the imaging case), it's useful to define a cartesian coordinate system fixed to the target. This coordinate system will move accordingly with the target as it maneuvers. Another assumption is that the target moves as a rigid body and that its instantaneous axis of rotation has a component $\hat{\mathbf{k}} \perp \hat{\mathbf{R}}$. To describe rotations of the target, we need to introduce a new reference frame by defining the directions $\hat{\mathbf{i}}$ and $\hat{\mathbf{j}}$ in terms of the rotation angle θ by $\hat{\mathbf{i}} \cdot \hat{\mathbf{R}} = \sin\theta$ and θ by $\hat{\mathbf{j}} \cdot \hat{\mathbf{R}} = \cos\theta$: these are the *cross-range* and *down-range* directions, respectively (see Figure 3).

Now using the new coordinates, equation (II.2) can be written as

$$\mathbf{H}_{scatt}(\mathbf{R}, t : k) = \frac{ik\mathbf{H}_0 e^{i(2kR - \omega t)}}{(2\pi)^3 R} \int_{\mathbb{V}} \rho_{k, \hat{\mathbf{R}}(x')} e^{i2k(y' \cos\theta - x' \sin\theta)} dx' dy' dz' \quad (\text{II.3})$$

and $\mathbf{x}' = x'\hat{\mathbf{i}} + y'\hat{\mathbf{j}} + z'\hat{\mathbf{k}}$. This is the standard target model used in radar imaging analysis. We know that $\rho_{k, \hat{\mathbf{R}}}$ depends on k and $\hat{\mathbf{R}}$, this dependence which is often treated as insignificant over the span of $\hat{\mathbf{R}}$, and the ranges of k obtainable from conventional radar systems. This dependence is typically ignored. This approximation allows us to exploit equation II.3 as a Fourier transform relationship between \mathbf{H}_{scatt} and $\rho \equiv \rho_{k, \hat{\mathbf{R}}}$. The Fourier transform is very convenient for practical object function estimation, but this approximation turns out to cause significant problems in image interpretation [Ref. 11].

Radar targets, especially man made targets, can be considered as a collection of point scatterers. The behavior of these scatterers has a vast variety of reflecting and back-scattering types. They can be edges, corners, circles, cavities, squares (see Figure 5)

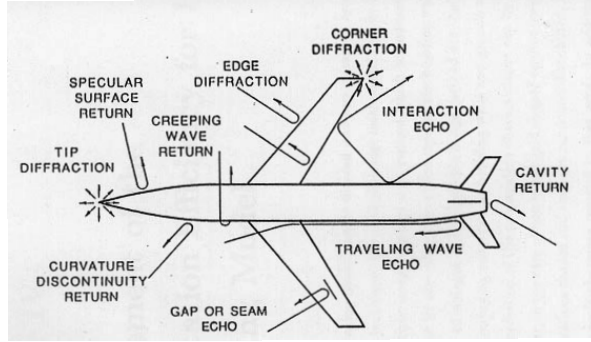


Figure 4. Scatter mechanism. This picture was taken from [Ref. 12]

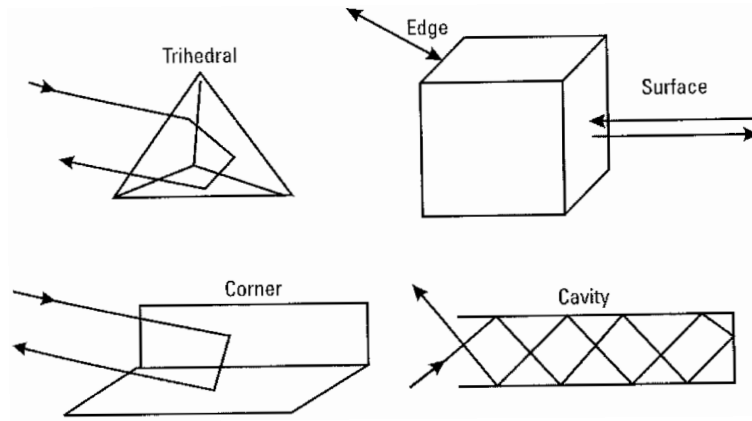


Figure 5. Different back-scattering behavior

B. SCATTERING FROM A SPHERE

To better understand how scattering depends on frequency let's introduce the simple example of scattering from a sphere. Assuming a plane harmonic wave of frequency ω (with $k = \frac{\omega}{c}$) and traveling along the z axis is incident on a perfectly conducting sphere of radius a . Let's determine the *physical optics* contribution to the scattered field and the associated scattering cross-section of the sphere with radius $r=1$.

$$\mathbf{H}_{scatt}(\mathbf{R}, t : k) = \frac{ik\mathbf{H}_0 e^{i(2kR - \omega t)}}{2\pi R} \int_{\hat{\mathbf{R}} \cdot \hat{\mathbf{n}} < 0} \hat{\mathbf{R}} \cdot \hat{\mathbf{n}} e^{i2k\hat{\mathbf{R}} \cdot \mathbf{x}'} dS' \quad (\text{II.4})$$

where $\hat{r} = \hat{n} = r \sin \theta \cos \phi \hat{i} + r \sin \theta \sin \phi \hat{j} + r \cos \theta \hat{k}$ (in spherical coordinates)

$$\hat{R} = \hat{k} \quad (\text{II.5})$$

$$\hat{n} \cdot \hat{R} = r \cos \theta = \cos \theta \quad (\text{II.6})$$

$$\hat{R} \cdot x' = \hat{R} \cdot a\hat{n} = a \cos \theta \quad (\text{II.7})$$

since just half of the sphere is visible

$$\int_{\hat{R} \cdot \hat{n} < 0} \hat{R} \cdot \hat{n} e^{ik \hat{R} \cdot x'} dS' = 2\pi a^2 \int_0^{\frac{\pi}{2}} \cos \theta e^{i2ka \cos \theta} \sin \theta d\theta \quad (\text{II.8})$$

Making now the substitution $\cos \theta = u$ and $-\sin \theta d\theta = du$ we obtain

$$\int_{\hat{R} \cdot \hat{n} < 0} \hat{R} \cdot \hat{n} e^{ik \hat{R} \cdot x'} dS' = 2\pi a^2 \int_0^{\frac{\pi}{2}} u e^{i2kau} du \quad (\text{II.9})$$

After some algebra we find the result of this integral to be

$$\int_{\hat{R} \cdot \hat{n} < 0} \hat{R} \cdot \hat{n} e^{ik \hat{R} \cdot x'} dS' = 2\pi a^2 \frac{1 - e^{i2ka} + 2e^{i2ka} ika}{i^2 4k^2 a^2} \quad (\text{II.10})$$

therefore

$$\mathbf{H}_{scatt}(\mathbf{R}, t : k) = -\frac{ik \mathbf{H}_0 e^{i(2kR - wt)}}{2\pi R} 2\pi a^2 \frac{1 - e^{i2ka} + 2e^{i2ka} ika}{4k^2 a^2} \quad (\text{II.11})$$

which reduces to

$$\mathbf{H}_{scatt}(\mathbf{R}, t : k) = \frac{i \mathbf{H}_0 a e^{i(2kR - wt)}}{4kaR} (1 - e^{i2ka} + 2e^{i2ka} ika) \quad (\text{II.12})$$

We define the radar cross-section σ by

$$\frac{\sigma}{\pi a^2} \approx \frac{|\mathbf{H}_{scatt}|^2}{|\mathbf{H}_0|^2} \frac{1}{\pi a^2} \quad (\text{II.13})$$

where \mathbf{H}_0 is the incident field [Ref. 11].

Figure 6 shows the basic regions characterizing the radar cross section of a sphere. The optical region (often called the *Fraunhofer region*) applies when $\frac{2\pi r}{\lambda} \gtrsim 10$. In this region, the *cross-section* is independent of frequency. At point *A* of Figure 6 we have a perturbation, the largest one, that would be 4 times higher than the cross section found in the optical region. A minimum also occurs at point *B* where the cross section would be 0.26 times the value in the optical region formula. This area is known as *Mie* or *resonance region*. There is another region where the diameter of the sphere is smaller than the wavelength: the *Rayleigh region*. As we can see, the cross-sectional is smaller than in the other regions and this happens because the wavelength is larger than the sphere, therefore, the scattered field in the direction of the sensor is very weak. *Rayleigh* scattering is important in weather radar. In our case we will be in the optical region because the bandwidth to be used in the test cases is from 8.75GHz-9.25Ghz. The wavelength is of the order of the order of 3cm, so, sufficient to detect parts of airplanes, ships, cars . As we saw in the

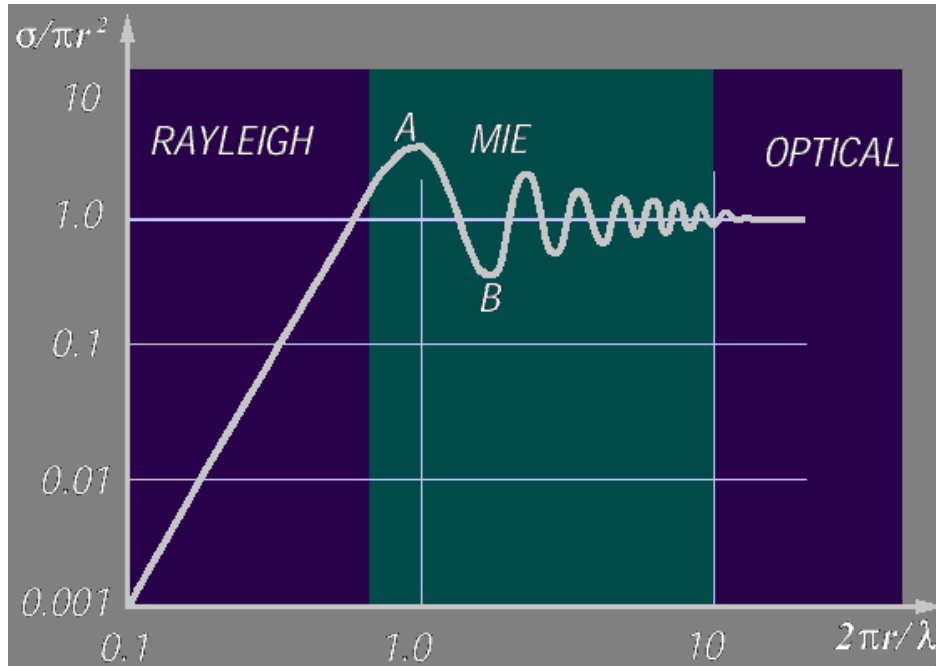


Figure 6. Coss-section plot on a log-log scale as a function of kr

weak-scatter far-field model, because we are in the optical region we will have some artifacts in the images crated by corner reflections, inlet engines and other types of undesired reflections from other geometrical shapes of the target.

C. IMAGING FROM WEAK-SCATTERER FAR-FIELD DATA USING FOURIER ANALYSIS

We can see from the weak-scatter far-field model of equation II.14 that the data is similar to a Fourier transform. In fact it is.

$$\{F\bar{\rho}_\theta\}(\omega) = \frac{1}{\sqrt{2\pi}} \int_{-\infty}^{\infty} \int_{-\infty}^{\infty} \rho(x, y) e^{i\omega(x\sin\theta - y\cos\theta)} dx dy \quad (\text{II.14})$$

In this approach we will take data over a small aperture $\Delta\theta$ with $0 \leq \theta \leq \Delta\theta \ll 1$. The small angle approximation $\sin\theta \approx \theta$ and $\cos\theta \approx 1$ implies

$$\{F\bar{\rho}_\theta\} \approx (\omega) \frac{1}{\sqrt{2\pi}} \int_{-\infty}^{\infty} \int_{-\infty}^{\infty} \rho(x, y) e^{i\omega(x\theta - y)} dx dy \quad (\text{II.15})$$

As we can see now the exponential in the equation II.15 has linear argument, since $k_x = \omega\theta$ and $k_y = \omega$ and so this equation can now be inverted using Fourier analysis: From the *frequency domain* data set $\{F\bar{\rho}_\theta\} \mapsto P(k_x, k_y)$, can be recovered as $\rho(x, y)$

$$\rho(x, y) = \frac{1}{2\pi} \int_{-\infty}^{\infty} \int_{-\infty}^{\infty} P(k_x, k_y) e^{i(k_x x - k_y y)} dk_x dk_y \quad (\text{II.16})$$

For reference purposes we switch x and y in the exponential argument from the weak-scatter far-field model and equation II.15 we label the *cross range* coordinate as x and the *down-range* coordinate as y .

The data set mapping $\{F\bar{\rho}_\theta\} \mapsto P(k_x, k_y)$ is based on the transformation $k_x = \omega\theta$ and $k_y = \omega$. If we consider $k_y = \omega$ to be a radial direction in the data space, then it's easy to see that $k_x = \omega\theta = K_y\theta$ is an arclength for fixed k_y . As was mentioned before, we are assuming small angles because our data set will be collected over a *small angle* grid in *polar coordinates* (see Figure 7).

We know that equation (II.16), on the other hand, is a two-dimensional Fourier

transform formula appropriate to data defined on a *rectangular grid* — that is, in this approach the data is processed on a rectangular grid but collected on a polar one [Ref. 11].

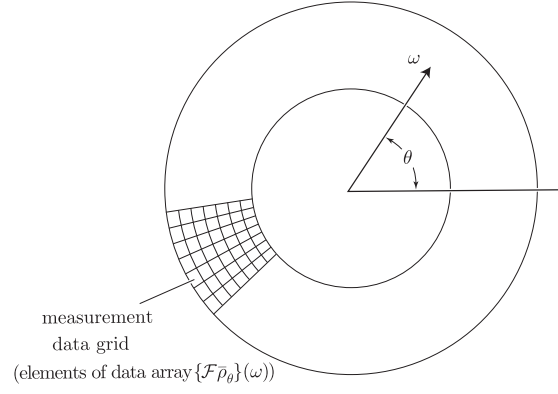


Figure 7. Data space used in the image recovery equation (II.16). Here $k_y = \omega$ is a polar direction and $k_y = \omega\theta$ is an arclength (for each ω). This picture was taken from [Ref. 11]

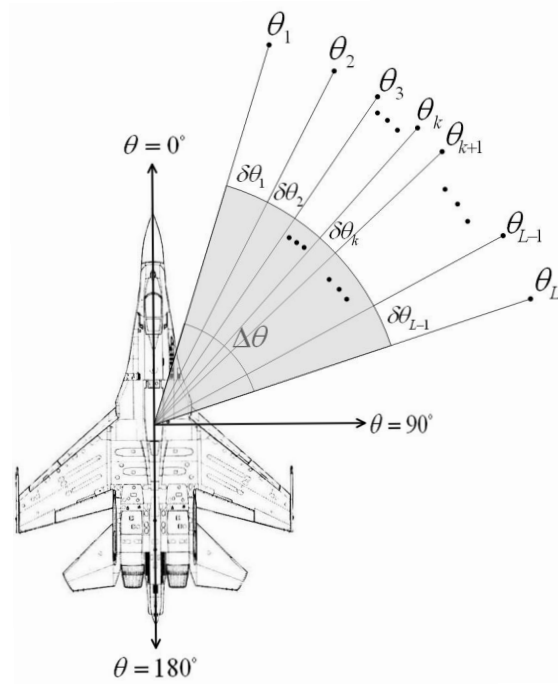


Figure 8. Radar Signals capture method. This picture was taken from [Ref. 12]

When ω is large and the aperture is sufficiently small, the polar grid is pretty close to rectangular in shape. But in the general case, the measured data must be interpolated to a rectangular grid before equation II.16 can be applied (an illustration is in Figure 9). In the radar community, this additional preprocessing step is known as *focussing* [Ref. 11].

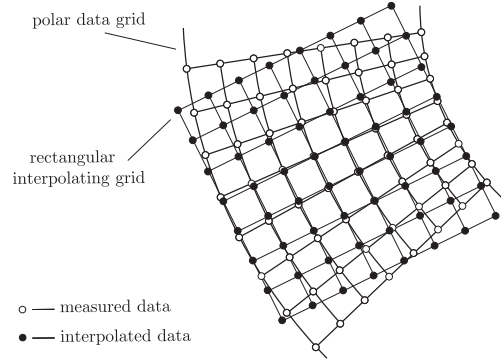


Figure 9. Data interpolation from a polar grid to a rectangular grid. This picture was taken from [Ref. 11]

One of the relevant aspects is the resolution of the image: equation (II.16) gives us the means to evaluate the resolution of the reconstructed image. This equation is the Fourier domain version of a convolution with an imaging kernel determined by the inverse Fourier transform of $k(k_x, k_y) = e^{i(k_x + k_y)}$.

Since we deal with finite bandwidth signals, the spatial-domain version of this imaging Kernel is a product of sinc functions and the width of the central lobes provides an estimate of the resolution. The dimensions Δx and Δy of a resolution cell can be estimated as

$$\Delta x \approx \frac{2\pi}{\Delta k_x} \approx \frac{2\pi}{\bar{\omega} \Delta \theta} \quad (\text{II.17})$$

$$\Delta y \approx \frac{2\pi}{\Delta k_y} \approx \frac{2\pi}{\Delta \omega} \quad (\text{II.18})$$

where $\bar{\omega}$ is the average frequency, $\Delta\theta$ represents the aperture size, and $\Delta\omega$ denotes the bandwidth[Ref. 11]. We can see that the *down-range* resolution depends on the bandwidth and the *cross-range* resolution depends on the aperture size, scaled by frequency. Don't forget we are using the small angle approximation and it's because of that assumption that this analysis is valid. This method will be used on test cases in the following chapters and analyzed concerning the pros and cons of this technique.

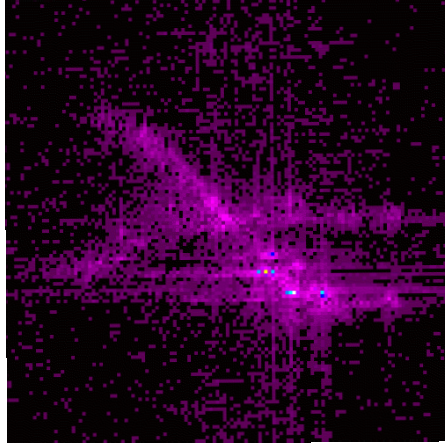


Figure 10. Standard Fourier image. This Figure was taken from [Ref. 13]

THIS PAGE INTENTIONALLY LEFT BLANK

III. RADON TRANSFORM

A. PRELIMINARY DISCUSSION

The objective of our work is to obtain range and cross range target information from *High Range Resolution* (HRR) data. To understand how to achieve this goal, let's examine a data model for an impulsive signal (ideal short pulse in time domain)

$$\eta(\tau, \nu) = \int_{-\infty}^{\infty} \int_{-\infty}^{\infty} \rho(\tau', \nu') \delta(\tau - \tau') e^{i\nu(\tau - \tau')} d\tau' d\nu' = \bar{\rho}(\tau) \quad (\text{III.1})$$

The HRR data are formed as the convolution between the first *range* argument of $\rho(\tau, \nu)$ with the measurement kernel (idealized by the delta function). In our case we want to distinguish range profiles by the target aspect angle at which the data are collected. Therefore,

$$\eta_{\theta}(\tau, \nu) = \int_{-\infty}^{\infty} \int_{-\infty}^{\infty} \rho_{\theta}(\tau', \nu') \delta(\tau - \tau') e^{i\nu(\tau - \tau')} d\tau' d\nu' = \bar{\rho}_{\theta}(\tau) \quad (\text{III.2})$$

since the scattering density function $\rho(\tau', \nu')$ will depend on target orientation (see Figure 11).

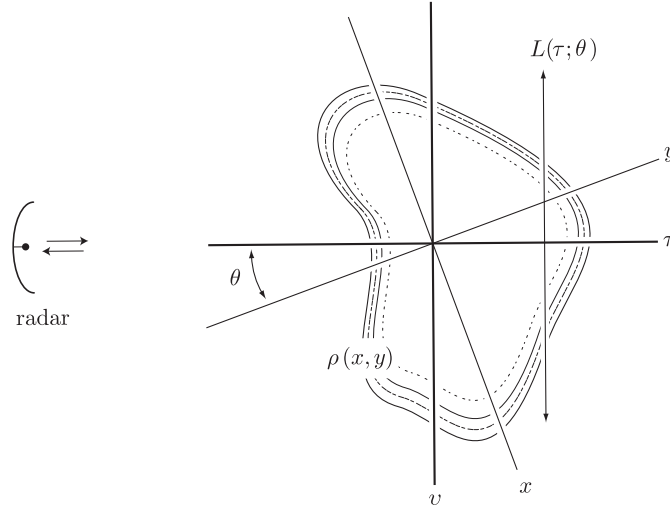


Figure 11. Geometry of an HRR profile at an angle θ . This picture was taken from [Ref. 11]

But the function $\rho_\theta(\tau', \nu')$ is just a rotated version of the stationary target. If we assume the coordinate system $x - y$ is fixed to the target and set the scattering density function in this coordinate system by

$$\rho(x, y) = \rho_{\theta=0}(\tau', \nu')$$

then for a general θ it's easy to see that,

$$\rho_\theta(\tau', \nu') = \rho(-\tau' \sin\theta + \nu' \cos\theta, \tau' \cos\theta + \nu' \sin\theta)$$

Using this result in equation III.3 yields

$$\eta_\theta(\tau, \nu) = \int_{-\infty}^{\infty} \int_{-\infty}^{\infty} \rho(-\tau' \sin\theta + \nu' \cos\theta, \tau' \cos\theta + \nu' \sin\theta) \delta(\tau - \tau') e^{i\nu(\tau - \tau')} d\tau' d\nu' = \bar{\rho}(\tau) \quad (\text{III.3})$$

Under the change in variables

$$\tau' = -x \sin\theta + y \cos\theta$$

$$\nu' = +x \cos\theta + y \sin\theta$$

equation III.3 becomes

$$\begin{aligned} \eta_\theta(\tau, \nu) &= \int_{-\infty}^{\infty} \int_{-\infty}^{\infty} \rho(x, y) \delta(\tau + x \sin\theta - y \cos\theta) e^{i\nu(\tau + x \sin\theta - y \cos\theta)} dx dy \\ &= \int_{-\infty}^{\infty} \int_{-\infty}^{\infty} \rho(x, y) \delta(\tau + x \sin\theta - y \cos\theta) dx dy \end{aligned} \quad (\text{III.4})$$

As we can see, this is just a *line integral* of $\rho(x, y)$ along the line $L(\tau; \theta)$ defined by $\tau + x \sin\theta - y \cos\theta = 0$ (because of the δ -function in the integrand). This line is illustrated in Figure 11. Note also that the argument of the complex exponential is zero and so doesn't contribute to the integral.

The $\eta_\theta(\tau, \nu)$ in equation III.4 is independent of ν and the double integral restricted to the line $L(\tau; \theta)$ or (the equivalent line integral itself) is known as the *Radon Transform* of $\rho(x, y)$ [Ref. 11],

$$\{R\rho\}(\tau, \theta) = \int_{-\infty}^{\infty} \int_{-\infty}^{\infty} \rho(x, y) \delta(\tau + x \sin\theta - y \cos\theta) dx dy \quad (\text{III.5})$$

The factor $\delta(\tau + x\sin\theta - y\cos\theta)$ is zero everywhere except where its argument is zero, which is along the straight line $x\sin\theta - y\cos\theta = \tau$. The straight line L represents a slit when it is at a perpendicular distance τ from the origin and inclined at an angle θ to the y-axis. If θ is kept fixed, say a value θ_1 while τ is varied, then the integral $\{R\rho\}(\tau, \theta_1)$ constitutes the projection of the density function $\rho(x, y)$ onto the line $\theta = \theta_1$ as a function of τ .

A practical computational method for inversion can be arrived at by Fourier transforming the Radon integral equation, finding a method of solution, and then transforming the steps to end up with a data-plane operations in which numerical Fourier transformation is actually dispensed with. The inversion procedure derives from a remarkable relation that exists between Fourier, Abel, and Hankel transforms and from a generalization known as the Projection-Slice Theorem[Ref. 5]. This theorem is discussed in the next section.

B. BACKPROJECTION

For every θ define $\{R\rho\}(\tau, \theta) = \bar{\rho}_\theta(\tau)$ of equation 11 to be a function of one variable τ then τ for each θ . The Fourier transform of $\bar{\rho}_\theta(\tau)$ can be computed as

$$\begin{aligned}
F\bar{\rho}_\theta(\omega) &= \frac{1}{\sqrt{2\pi}} \int_{-\infty}^{\infty} \bar{\rho}_\theta(\tau) e^{i\omega\tau} d\tau \\
&= \iiint_{-\infty}^{\infty} \rho(x, y) \delta(\tau + x\sin\theta - y\cos\theta) e^{i\omega\tau} d\tau dx dy \\
&= \iint_{-\infty}^{\infty} \rho(x, y) e^{i\omega(x\sin\theta - y\cos\theta)} dx dy \\
&= \iint_{-\infty}^{\infty} \rho(x, y) e^{i(k_x x - k_y y)} dx dy
\end{aligned} \tag{III.6}$$

assuming $k_x \equiv -\omega\sin\theta$ and $k_y \equiv \omega\cos\theta$.

We observe that equation III.6 corresponds to a 2D Fourier transform of the density function $\rho(x, y)$. As is well known, the 2D Fourier transform is given by

$$P(k_x, k_y) = \frac{1}{2\pi} \int_{-\infty}^{\infty} \int_{-\infty}^{\infty} \rho(x, y) e^{i(k_x x - k_y y)} dx dy \tag{III.7}$$

and so we can conclude

$$P(-\omega \sin \theta, \omega \cos \theta) = \frac{1}{\sqrt{2\pi}} F \bar{\rho}_\theta(\omega) \quad (\text{III.8})$$

Equation III.8 is known as the *Projection-Slice Theorem*, and allows us to determine $\rho(x, y)$ from the inverse Fourier transform of $F(k_x, k_y)$. We can use this result to build an inverse Radon transform for $\bar{\rho}(\tau, \theta)$. Using the change of variables $(k_x, k_y) \mapsto (\omega, \theta)$ where $k_x \equiv -\omega \sin \theta$ and $k_y \equiv \omega \cos \theta$, we obtain

$$\begin{aligned} \rho(x, y) &= \frac{1}{2\pi} \iint_{-\infty}^{\infty} P(k_x, k_y) e^{i(k_x x - k_y y)} dk_x dk_y \\ &= \frac{1}{(2\pi)^{3/2}} \int_0^{2\pi} \int_{-\infty}^{\infty} F \bar{\rho}_\theta(\omega) e^{-i\omega(x \sin \theta - y \cos \theta)} \frac{\partial(k_x, k_y)}{\partial(\omega, \theta)} d\omega d\theta \\ &= \frac{1}{(2\pi)^{3/2}} \int_0^{2\pi} \int_{-\infty}^{\infty} F \bar{\rho}_\theta(\omega) e^{-i\omega(x \sin \theta - y \cos \theta)} |\omega| d\omega d\theta \\ &= \frac{1}{(2\pi)^{3/2}} \int_0^{2\pi} \int_{-\infty}^{\infty} \left(|\omega| F \bar{\rho}_\theta(\omega) \right) e^{i\omega(-x \sin \theta + y \cos \theta)} d\omega d\theta \end{aligned} \quad (\text{III.9})$$

The inner integral of equation III.9 is just the inverse Fourier transform of the product

$$Q(\omega) \equiv \omega \times \{F \bar{\rho}_\theta(\omega)\}$$

The inverse Fourier transform of $Q(\omega)$ is

$$q(t) = \frac{1}{\sqrt{2\pi}} \int_{-\infty}^{\infty} Q(\omega) e^{i\omega t} d\omega$$

and so the equation III.9 can be written as

$$\rho(x, y) = \frac{1}{\sqrt{2\pi}} \int_0^{2\pi} q(-x \sin \theta + y \cos \theta) d\theta \quad (\text{III.10})$$

where after substitution of $F \bar{\rho}_\theta(\omega)$, we obtain

$$q(t) = \frac{1}{2\pi} \int_{-\infty}^{\infty} \int_{-\infty}^{\infty} \bar{\rho}_\theta(\tau) |\omega| e^{i\omega(t-\tau)} d\omega d\tau \quad (\text{III.11})$$

Equation III.10 is called the *backprojection operator* and the *filtered backprojection algorithm* combines equations III.10 and III.11 to form the an inverse Radon transform $\bar{\rho}(\tau, \theta) = \bar{\rho}(\tau) \rightarrow \rho(x, y)$.

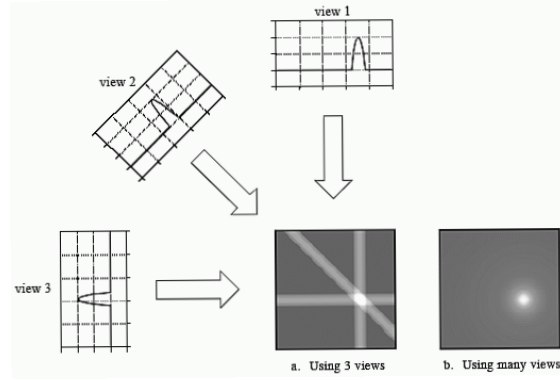


Figure 12. Backprojection reconstructs an image by taking each view and *smearing* it along the path it was originally acquired. The result image is a blurry version of the correct image. This picture was taken from [Ref. 15]

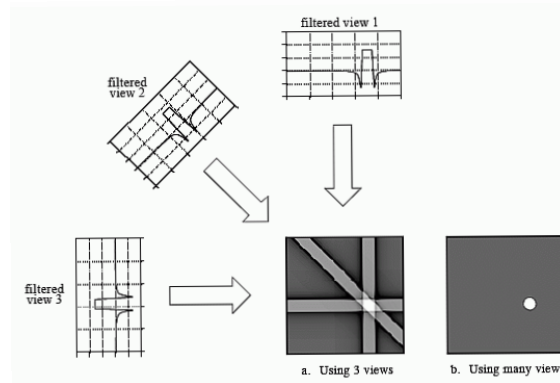


Figure 13. Filtered backprojection reconstructs an image by filtering each view before backprojection. This removes the blurring seen in simple backprojection, and results in a mathematically exact reconstruction of the image. Filtered backprojection is the most commonly used algorithm for computed tomography systems. This picture was taken from [Ref. 15]

THIS PAGE INTENTIONALLY LEFT BLANK

IV. TIME-FREQUENCY METHODS

A. ISAR IMAGING USING TIME FREQUENCY TECHNIQUES

The approach to Inverse synthetic aperture radar (*ISAR*) is exactly the same as for SAR, but in ISAR we exploit the target's motion. The goal is to generate images of moving targets in the range-Doppler plane. Usually the Fourier transform is used to compute the image, but because of the unpredictable movement of the target the Doppler-frequency can display nonuniform time variations. To overcome this time-varying Doppler spectrum we investigate the use of a time-frequency transform.

In this thesis we will examine the performance of two different transforms, the short time Fourier transform itself and the wavelet transform to obtain ISAR images. Time-frequency techniques are used to overcome limitations of the standard Fourier transform. For example, during the collection of data the scattering points must remain in the same range cell: if this doesn't happen, the image will be blurred. This occurs when scatterers move out of their range cells making our Doppler information non-linear. Since the Fourier transform requires linear sampling, we can't compensate for this effect. To obtain a focussed radar image using the Fourier transform, motion compensation algorithms are necessary to adjust for scatterer migration. But this is often not enough because the spectrum can still display non-linear behavior. So, Doppler tracking and other techniques must be applied. When a target is moving smoothly, these standard techniques are normally good enough to focus our image and we can still use the Fourier transform. However, when the target exhibits unexpected motion, such as rapid maneuvers and acceleration about an axis, the standard motion compensation algorithms are not enough to focus the image. In this situation, more advance algorithms for motion compensation are needed [Ref. 16]. However, such advanced algorithms are not always effective against the image blurring, because the scatterers may still drift out of their range cells and, as a consequence, their Doppler

frequency shifts become nonlinear in time. Therefore the image will still come out blurred after the Fourier transform.

As a matter of fact, the Fourier transform limitations can be mitigated using the *Short Time Fourier Transform* (STFT). As we explained before, the Doppler information is nonlinear with time, therefore a good method to solve the smeared Fourier frequency spectrum is to apply high-resolution time-frequency transform to the processing. Using this method, we no longer need the motion compensation algorithms because we are no longer using the Fourier transform. This way, unpredictable Doppler frequency shifts can be overcome without using sophisticated motion compensation algorithms. The use of the STFT will be the first to be applied to our case. In the same way, another frequency analysis tool can be applied using the *Continuous Wavelet transform* (CWT). The wavelet approach offers an alternative path for signal processing. Essentially, the CWT is the same as the STFT except that any basis functions can be used (only harmonic functions of constant amplitude and phase are used by the STFT [Ref. 17]). Another difference between the CWT and the STFT is the window size: the STFT uses one window analysis with the same width, while the CWT uses different windows for different frequencies. (Short windows for high frequencies and long windows for low frequencies.)

1. Short Time Fourier Transform vs. Continuous Wavelet transform

In the standard FT we assume signals of infinite length with stationary spectrum, thus making it not well suited to the detection of time varying spectra. The STFT on the other hand computes the FT of the signal on a window sliding in time, thus capturing the non-stationary behavior. The STFT is defined in the following way

$$STFT(t, \nu) = \int_{-\infty}^{\infty} s(\tau) w(\tau - t) e^{-i\nu\tau} d\tau \quad (\text{IV.1})$$

The window $w(\tau - t)$ is centered on the time variable t and then shifted the window through out the signal to obtain the information about the frequency behavior in time

(see Figure 14) . As far as its application to imaging is concerned STFT is affected by the uncertainty principle by which the signal cannot be resolved in both time and frequency (see Figure 15 and Figure 16). Also, the STFT is only a window-averaged frequency spectrum and not an exact estimation of the instantaneous frequency [Ref. 18].

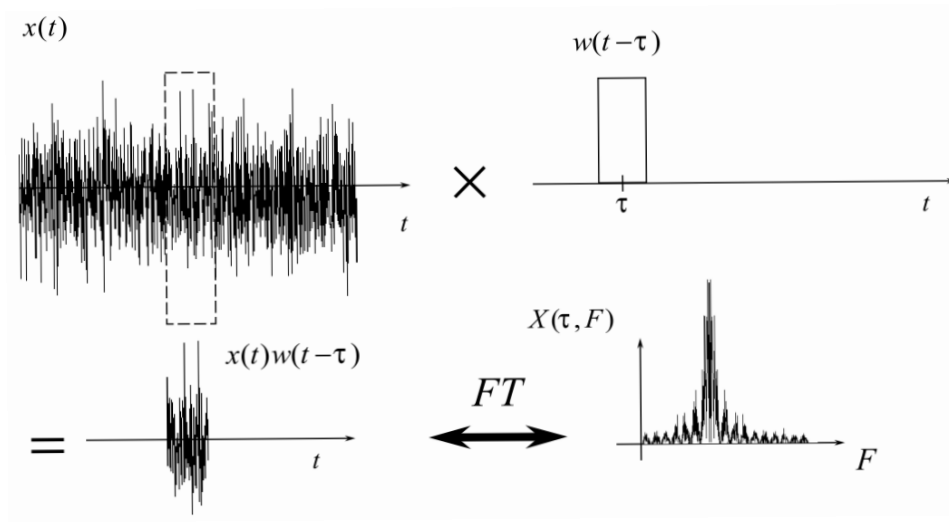


Figure 14. Short time Fourier Transform. This figure was taken from [Ref. 10]

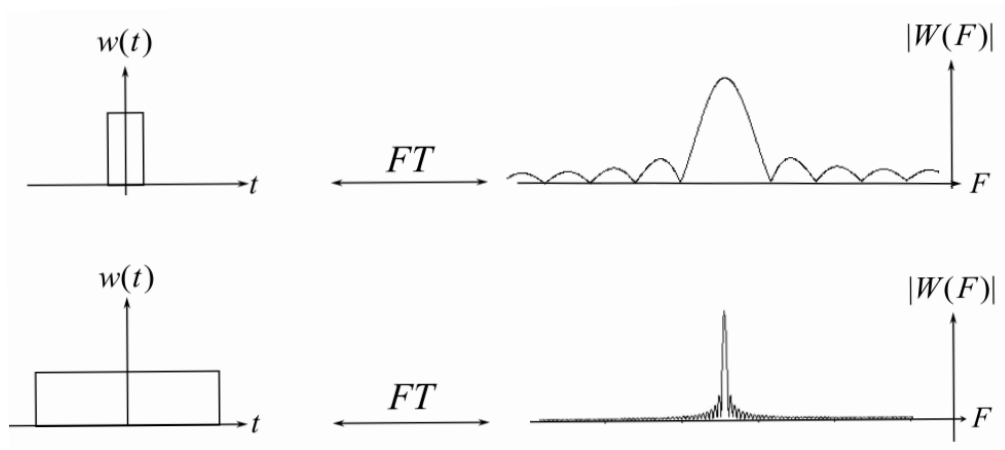


Figure 15. Time/frequency uncertainty of a rectangular window. This figure was taken from [Ref. 10]

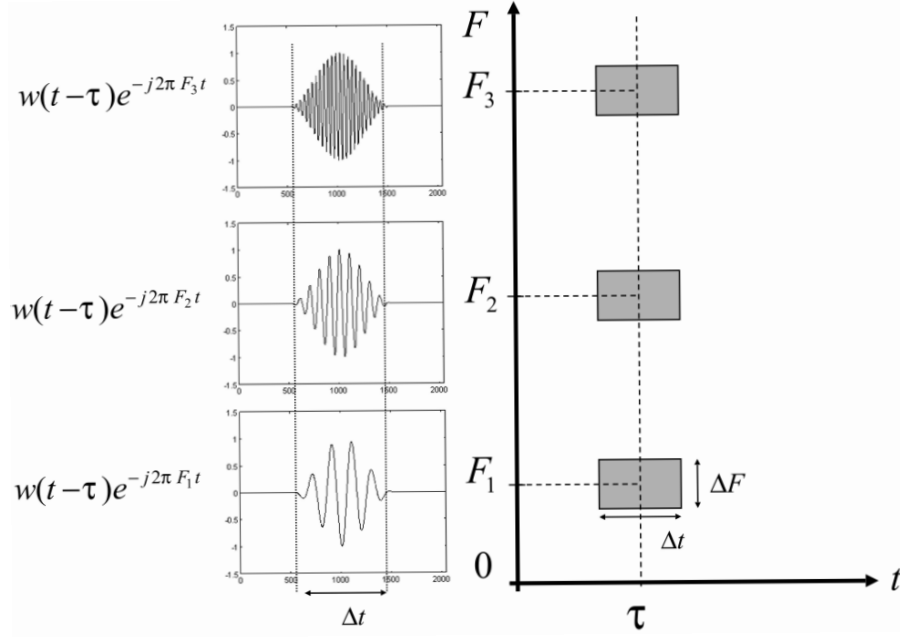


Figure 16. Basis functions and time/frequency resolution for STFT. This figure was taken from [Ref. 10]

The best compromise is to have different resolutions at different frequencies by adapting the window length in time. This is what the CWT tries to accomplish.

$$CWT(\tau, \alpha) = \int_{-\infty}^{\infty} x(t) \alpha^{0.5} \psi(\alpha(t - \tau)) dt \quad (\text{IV.2})$$

As we saw before, the STFT has a fixed-length window which is responsible for the principal limitation of time and frequency resolution due to the uncertainty principle. Either we resolve in time or we resolve in frequency. In order to circumvent this issue, we will observe the signal using different window-lengths because the CWT allows it. Normally we are interested in the higher frequencies due to rapid function variation as a function of time. Evidently, it makes some sense to use a long window for low frequencies and a short window for high frequencies to get high resolution over all spectrum specially at higher frequencies.

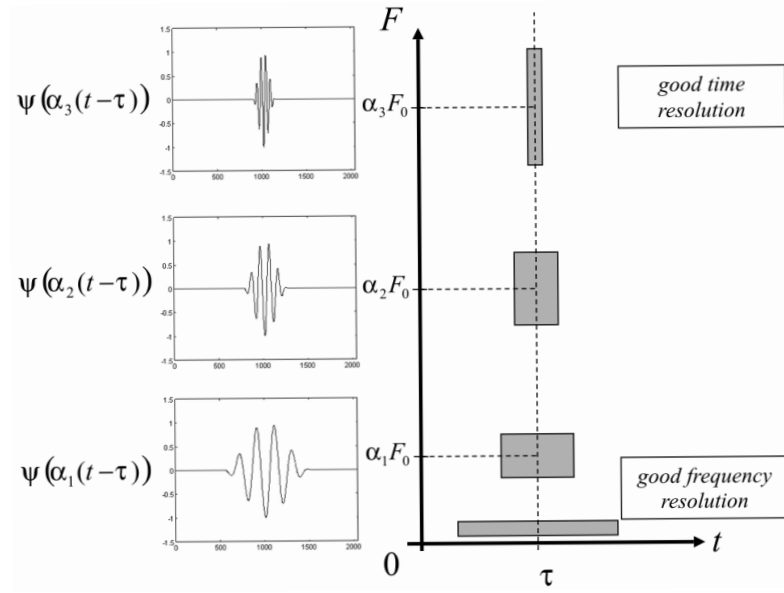


Figure 17. Basis functions and time/frequency resolution for CWT. This figure was taken from [Ref. 10]

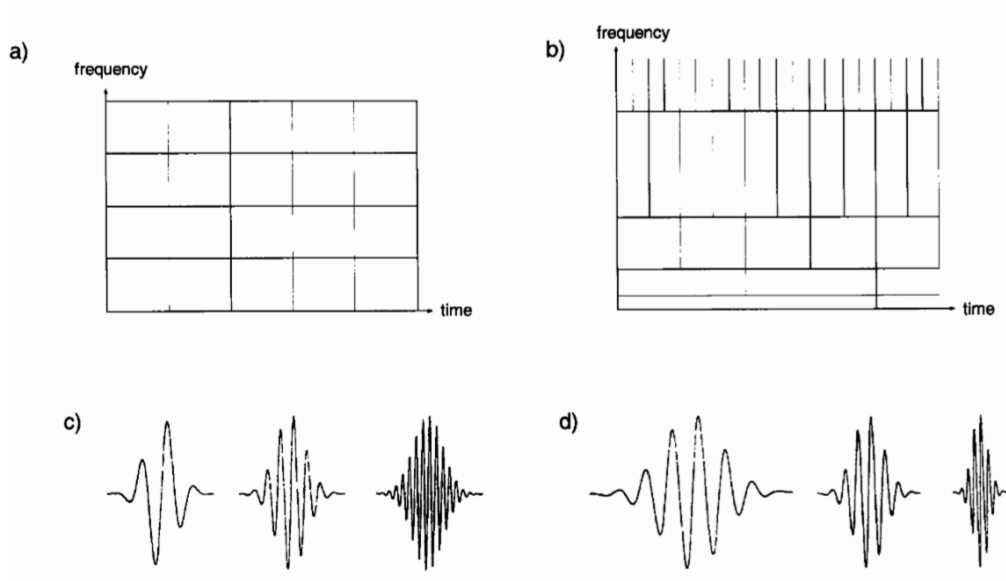


Figure 18. Basis functions and time/frequency resolution of the STFT and the CWT. The tiles represent for a given basis functions its concentration in the time-frequency plane. a) Coverage of the time-frequency plane for the STFT. b) for the CWT c) Corresponding basis functions for the STFT. d) for the CWT. This figure was taken from [Ref. 19]

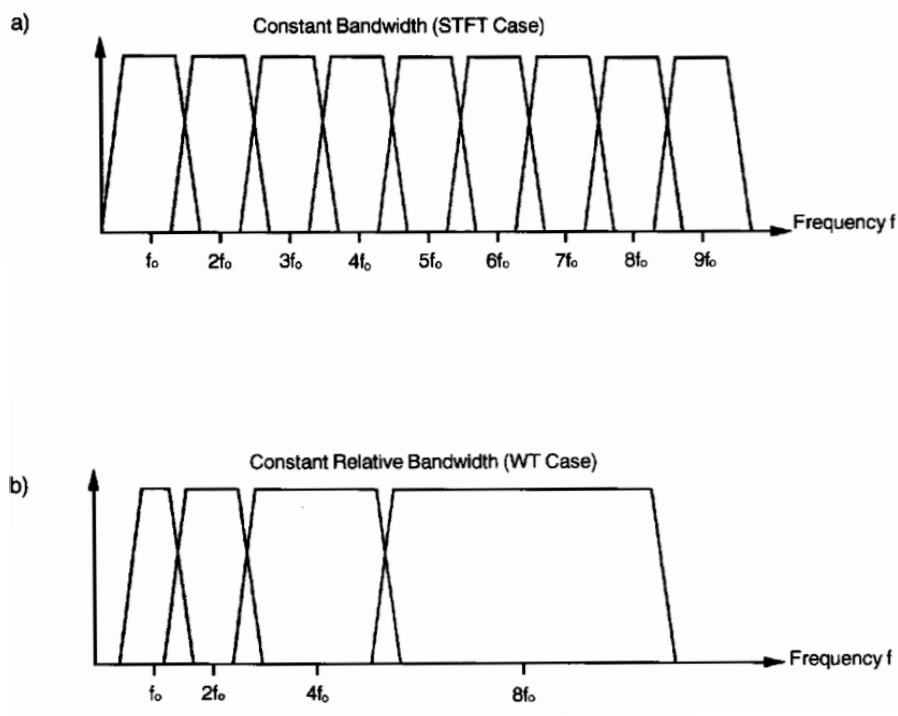


Figure 19. Division of the frequency domain a) for the STFT (uniform coverage) and b) for CWT (logarithmic Coverage). This figure was taken from [Ref. 19]

B. EXAMPLE OF A CHIRP USING STFT VS. CWT

We present in Figures 20 and 21 a spectrogram and a scalogram from a chirp signal of length 2000 samples, where the frequency grows continuously and linearly. The spectrogram is obtained using a Gaussian-like window and the scalogram is obtained with a Morlet wavelet (a complex sinusoid windowed with a Gaussian envelope). In this way, we can see that for the STFT the width of the frequency line is always the same as a result of the constant window width and the uniform coverage in the frequency domain. However, the scalogram with nonlinear (logarithmic) scale results in a curve instead of a line. Also, we can see that the width of the line is thinner for high frequencies, a result that reflects the long duration windows in time for higher frequencies.

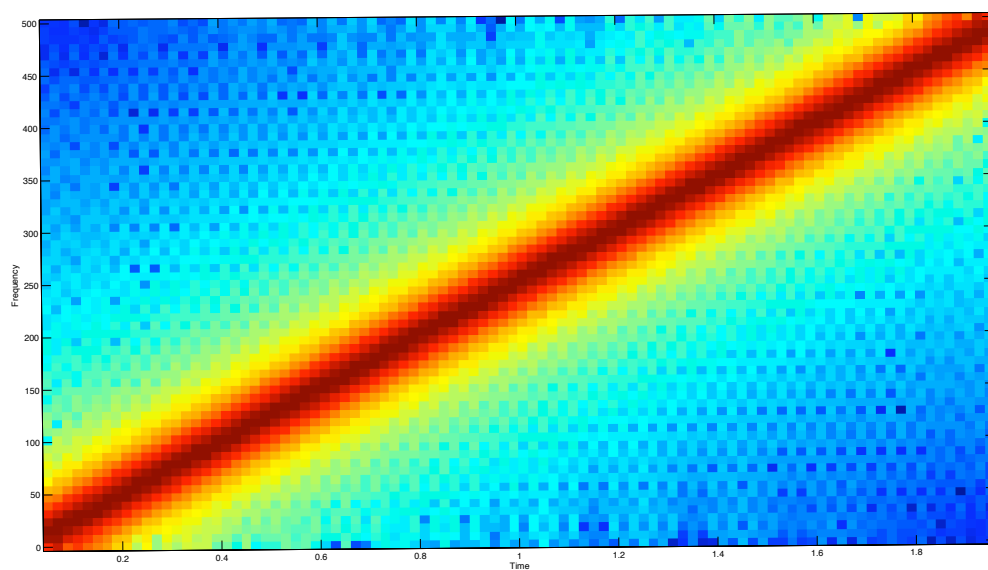


Figure 20. Chirp's Spectrogram

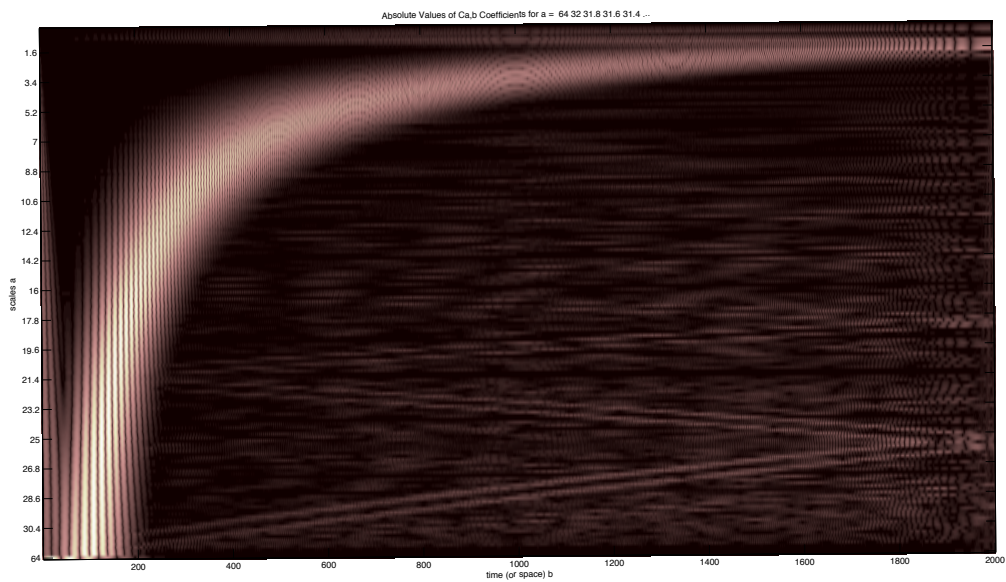


Figure 21. Chirp's Scalogram

THIS PAGE INTENTIONALLY LEFT BLANK

V. ISAR IMAGING USING STFT AND CWT

A. BACKHOE DATA DOME

To further examine the potential of using time-frequency methods to produce ISAR images, we examined simulated data based on the Air Force Research Laboratory (AFRL), Backhoe Data Dome, Version 1.0.

1. Backhoe Data Dome Version 1.0

The Backhoe Data Dome, Version 1.0 consists of simulated wideband (7-13 GHz), full polarization, complex backscatter data from a backhoe loader generated using a Computer-Aided-Design (CAD) model in free space as shown in Figure 22. The MATLAB program *plotfacet.m* available from the Air Force Research Laboratory Sensor Data Management System was used to plot all 3-D graphics of the backhoe loader.



Figure 22. CAD Model of Backhoe Loader

The backscatter data consists of over 1,125 Matlab binary files (*.mat files) in which each file has the k - space data from with elevation between 18 and 42 degrees and Azimuth between 66 and 114 degrees. The filenames are indicative of the data they contain. *backhoe-el042-az109.mat*, for example, contains the data with elevation between 29.5 and 30.5 and azimuth between 89.5 and 90.5. The viewing hemisphere consists of 14 samples per degree in both azimuth and elevation. There

is one sample every 11.75 MHz over the 6 GHz bandwidth and full polarization information; i.e. horizontal linear polarization on transmit and receive (HH), vertical linear polarization on transmit and receive (VV), and horizontal linear polarization on transmit and vertical linear polarization on receive (HV).

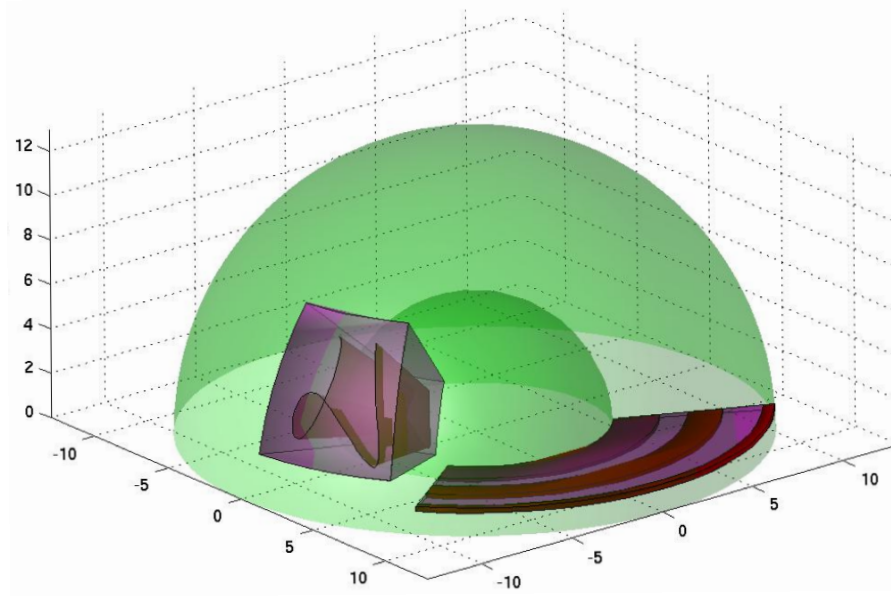


Figure 23. Backhoe Data Dome Representation in k-Space

With the methods described in the preceding Chapters, the STFT and CWT will be applied to the 3-D k-space data for the different test cases, with the following setup in the following orientations and using the specified polarization:

Test Case 1: Data collected over the following interval (horizontal Path): Elevation=42deg and $95\text{deg} \leq \text{Azimuth} \leq 102\text{deg}$.

Test Case 2: Data collected over the following interval (curve Path): $38 \leq \text{Elevation} \leq 42\text{deg}$ and $95\text{deg} \leq \text{Azimuth} \leq 99\text{deg}$.

In all cases the center frequency chosen was 9.25GHz with a Bandwidth of 500 MHz. We chose 500 MHz because it's a more realistic case, and is representative of existing radars in the world. With respect to Polarization, this will not be very important in our simulation but, of course, Polarization matters in the case we have a Radar with cross-polarization capabilities. In this case, the amount of information available to reconstruct the image will be greater than with just vertical or horizontal polarization. Cross-pol images will be briefly analyzed below.

B. ALGORITHM FOR ISAR IMAGING USING TIME-FREQUENCY METHODS

After the complex data is extracted from our database, we construct a matrix in which the N columns have the range information and the M rows have the cross-range information.

step 1. We do the *Fast Fourier Transform* of the rows to obtain our range profiles. For each row $X(l) = FFT[x_i(n)], n = 1, 2, \dots, N; i = 1, 2, \dots, M$.

step 2. Compute the STFT or CWT using different windows type, sizes and scales. $Y(m) = STFT[y_i(n)]$ or $Y(m) = CWT[y_i(n)], n=1,2,\dots,N; i=1,2,\dots,M$.

step 3. Find the absolute value for each entry of the matrix and plot it.

Step 1 to 3 form the algorithm for ISAR imaging using the two time-frequency methods: first *Short Time Fourier Transform*; and second the *Continuous Wavelet Transform*.

C. TEST CASE 1 : $95^\circ \leq \theta_{AZIMUTH} \leq 102^\circ, \phi_{ELEVATION} = 42^\circ$

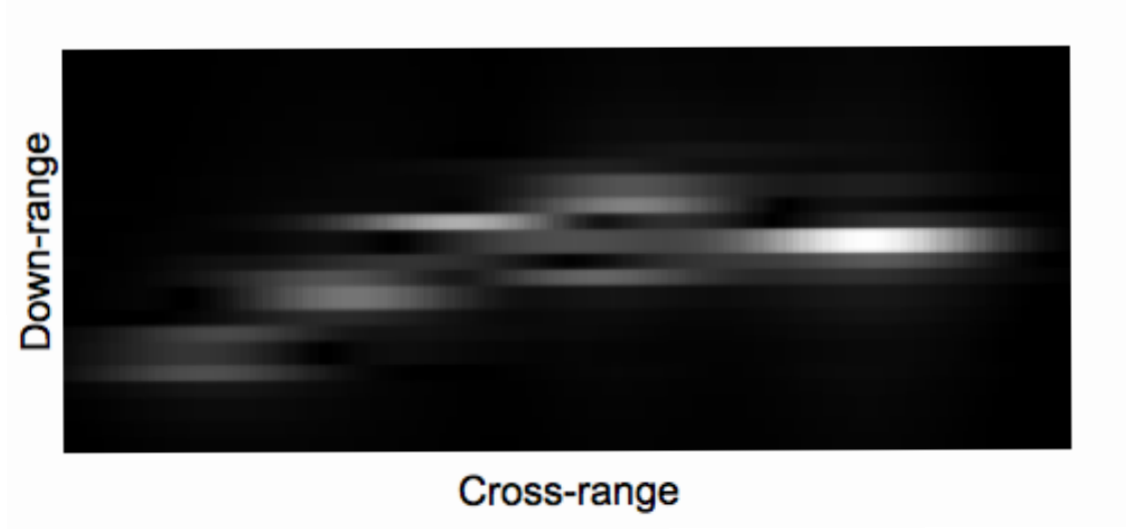


Figure 24. ISAR image using STFT with a hamming window with 20 points of size and 50% of overlapping (Horizontal Polarization) - (9^{th} frame)

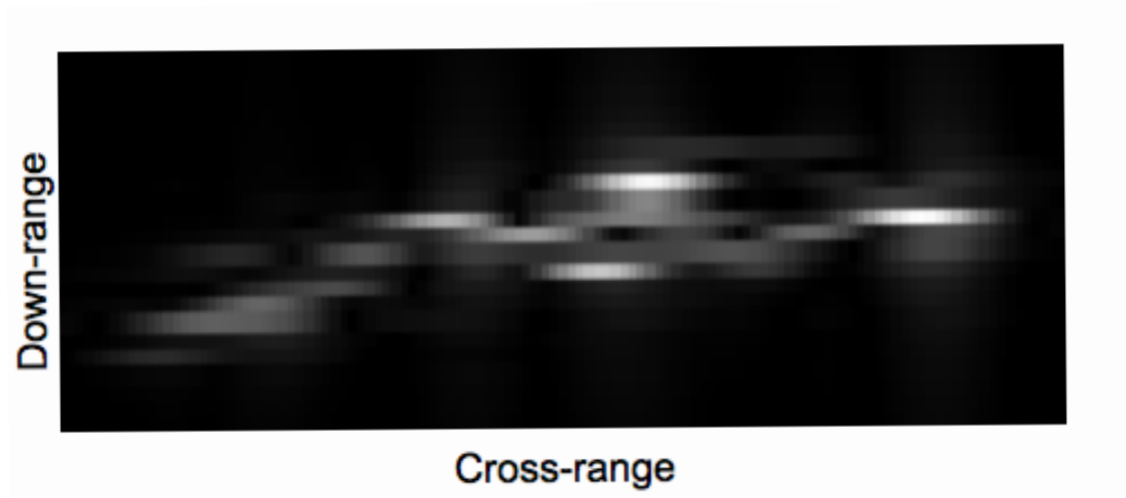


Figure 25. ISAR image using STFT with a hamming window, size 40 points and 50 percent of overlapping (Horizontal Polarization) - (2^{th} frame)

We can already observe that when we increase the window size the image is going to display better resolution.

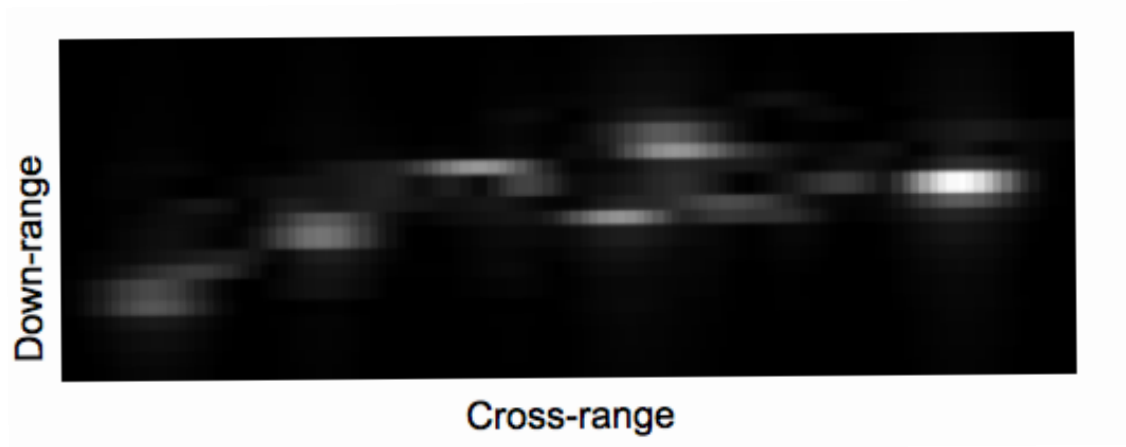


Figure 26. ISAR image using STFT with a hamming window, size 50 points and 50 percent of overlapping (Horizontal Polarization) - (3^{th} frame)

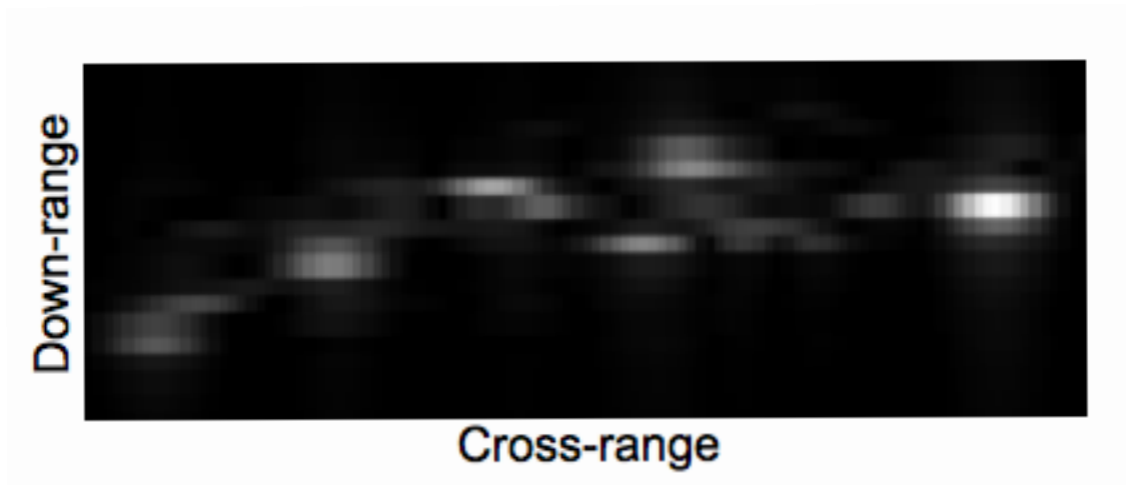


Figure 27. ISAR image using STFT with a hamming window, size 60 points and 50 percent of overlapping (Horizontal Polarization) - (2^{th} frame)

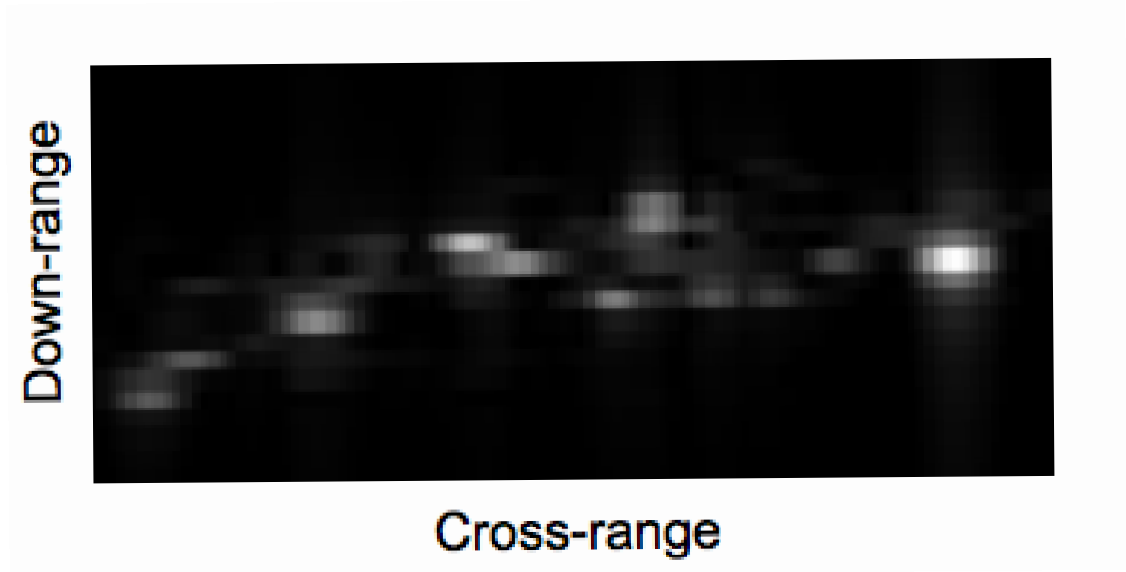


Figure 28. ISAR image using STFT with a hamming window, size 80 points and 50 percent of overlapping (Horizontal Polarization) - (1^{th} frame)

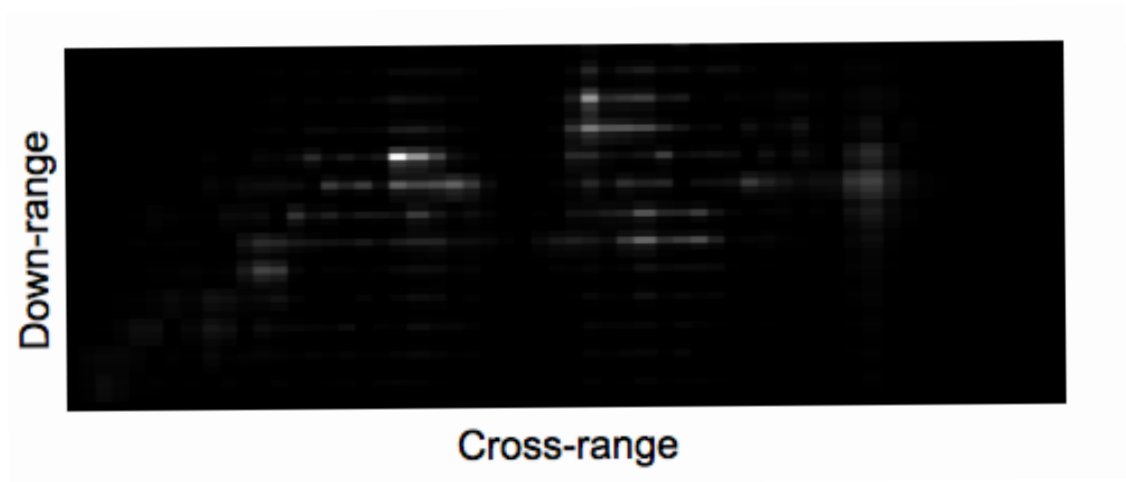


Figure 29. ISAR image using CWT with a mexican hat window, using a scale of 1:5 (Horizontal Polarization)

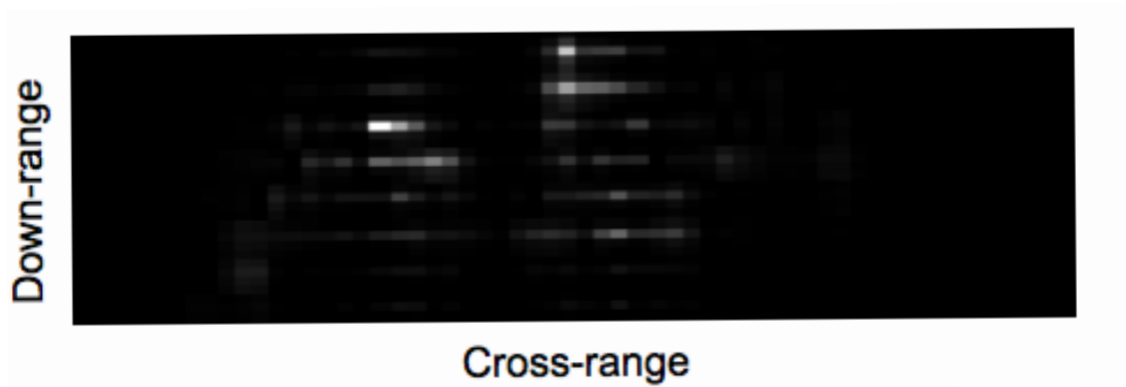


Figure 30. ISAR image using CWT with a mexican hat window, using a scale of 3:6 (Horizontal Polarization)

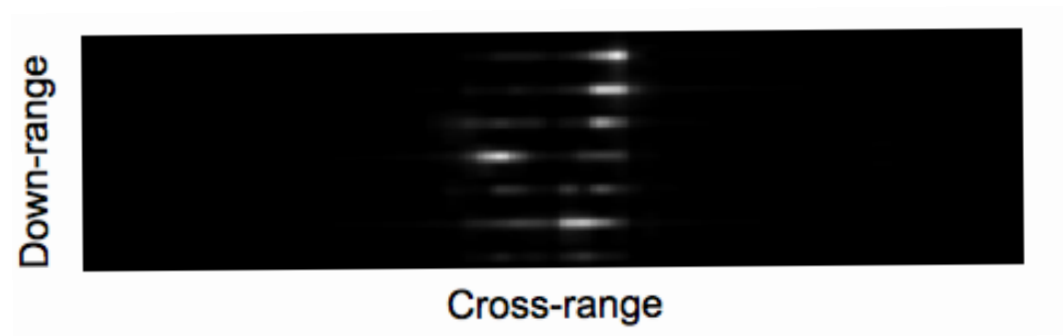


Figure 31. ISAR image using CWT with a mexican hat window, using a scale of 10:13 (Horizontal Polarization)

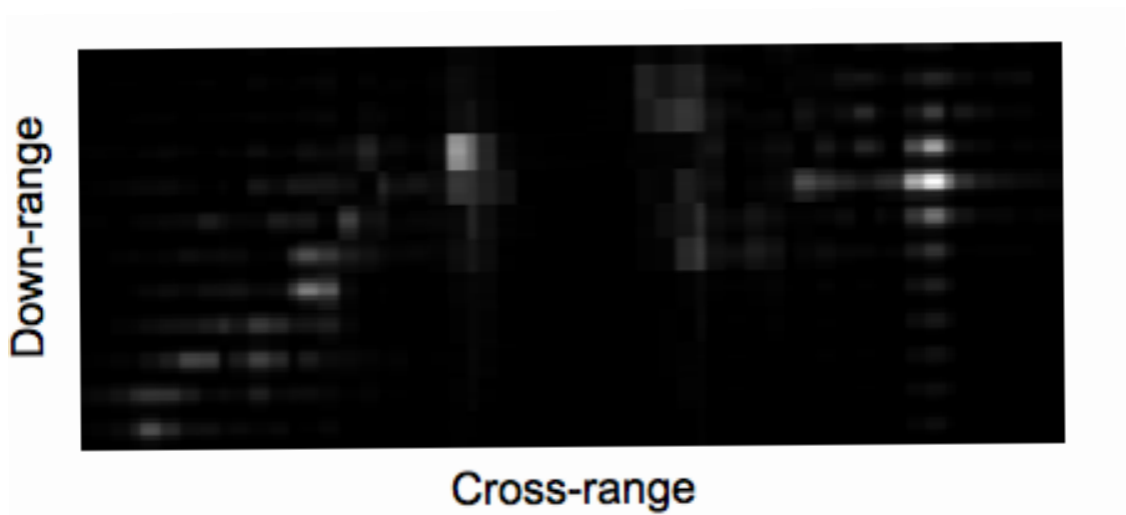


Figure 32. ISAR image using CWT with a Morlet window (Horizontal Polarization)

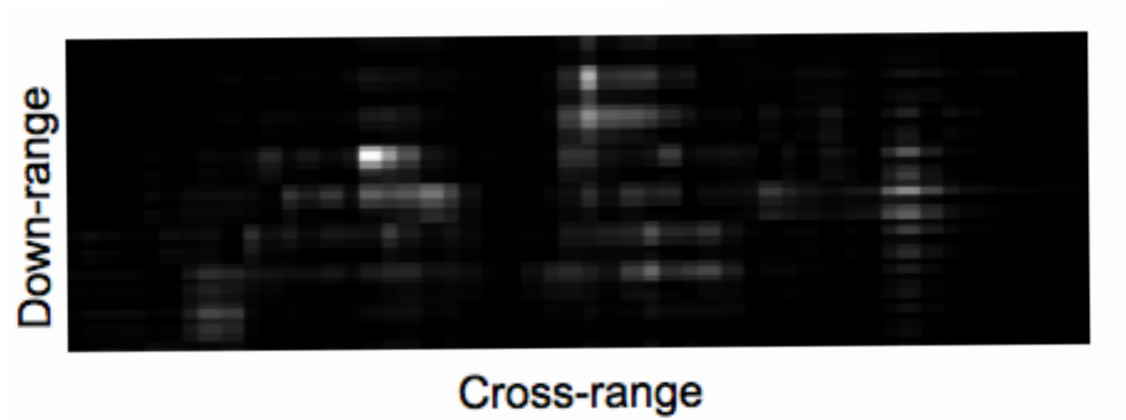


Figure 33. ISAR image using CWT with a Daubechies 2 window (Horizontal Polarization)

D. TEST CASE 2 : $38 \leq \text{ELEVATION} \leq 42\text{DEG}$ AND $95\text{DEG} \leq \text{AZIMUTH} \leq 99\text{DEG}$.

When we use STFT we'll observe the resolution increasing when we increase the window's size. When we use CWT we can observe that when we change scale we can loose information or improve the resolution of the STFT approach.

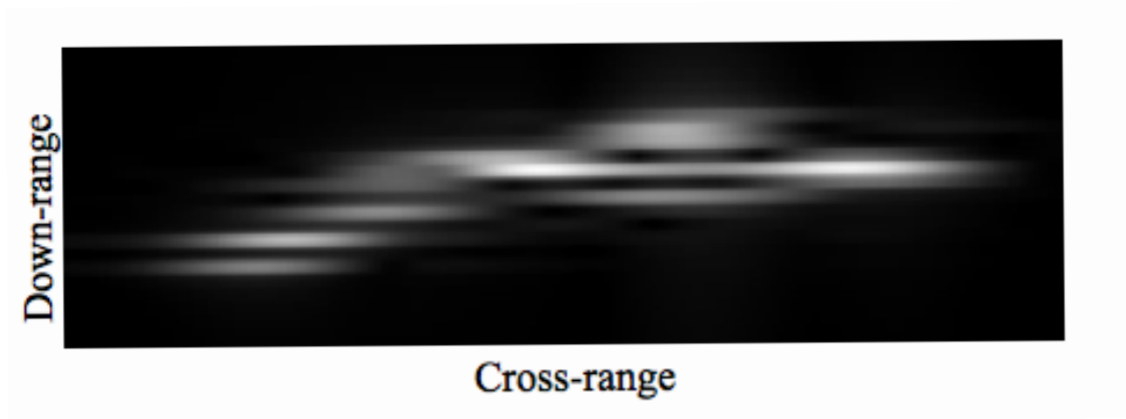


Figure 34. ISAR image using STFT with a hamming window, size 20 points and 50 percent of overlapping (Horizontal Polarization) - (8th frame)

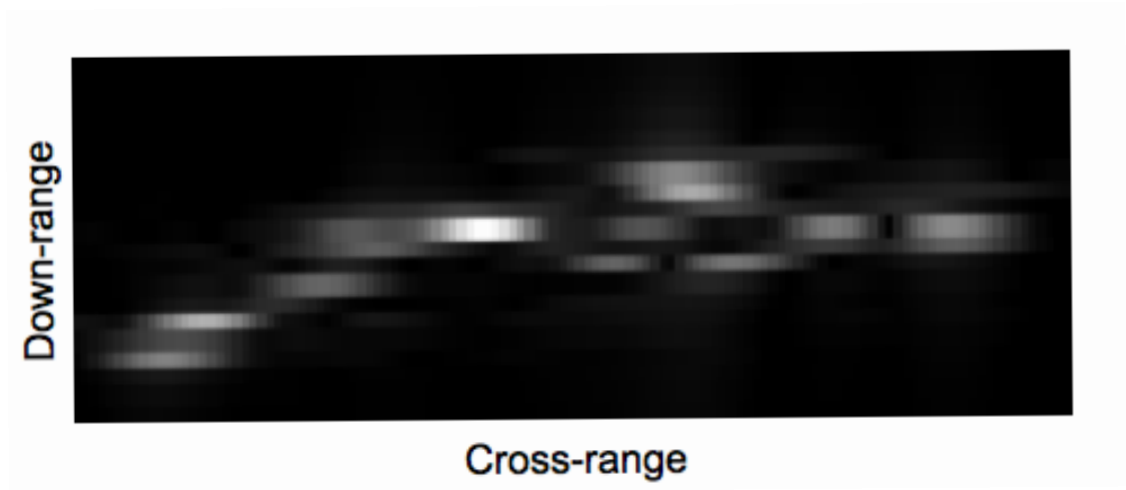


Figure 35. ISAR image using STFT with a hamming window, size 40 points and 50 percent of overlapping (Horizontal Polarization) - (3^{th} frame)

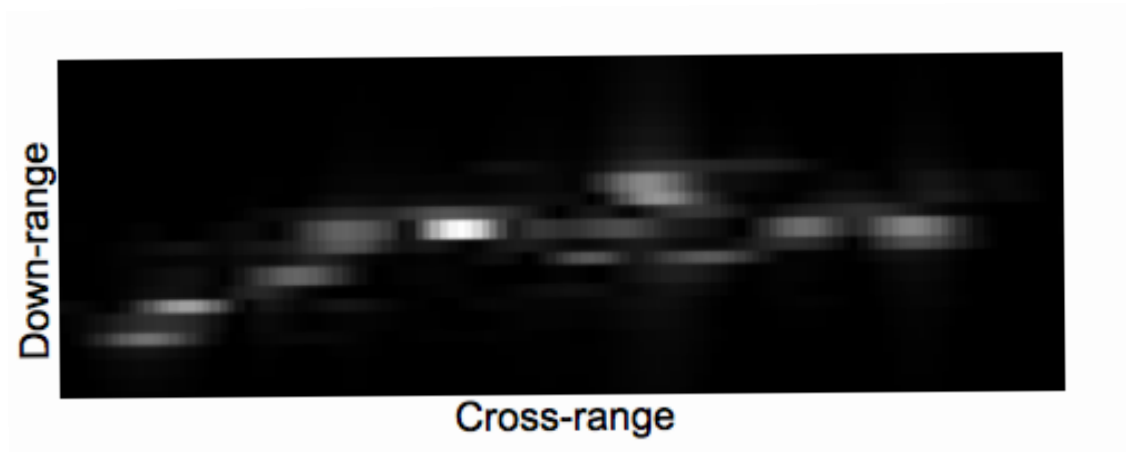


Figure 36. ISAR image using STFT with a hamming window, size 50 points and 50 percent of overlapping (Horizontal Polarization) - (2^{th} frame)

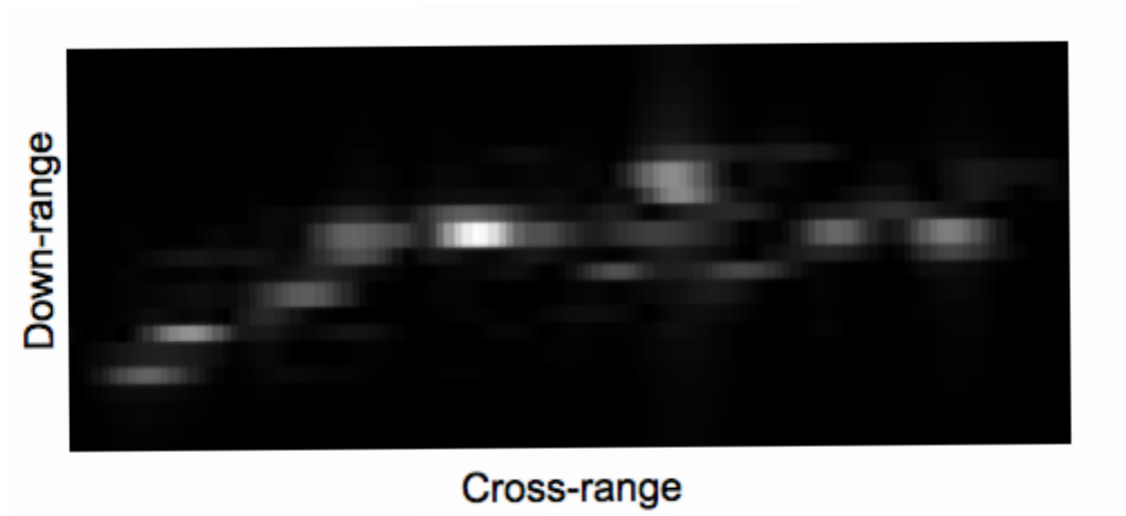


Figure 37. ISAR image using STFT with a hamming window, size 60 points and 50 percent of overlapping (Horizontal Polarization) - (2^{th} frame)

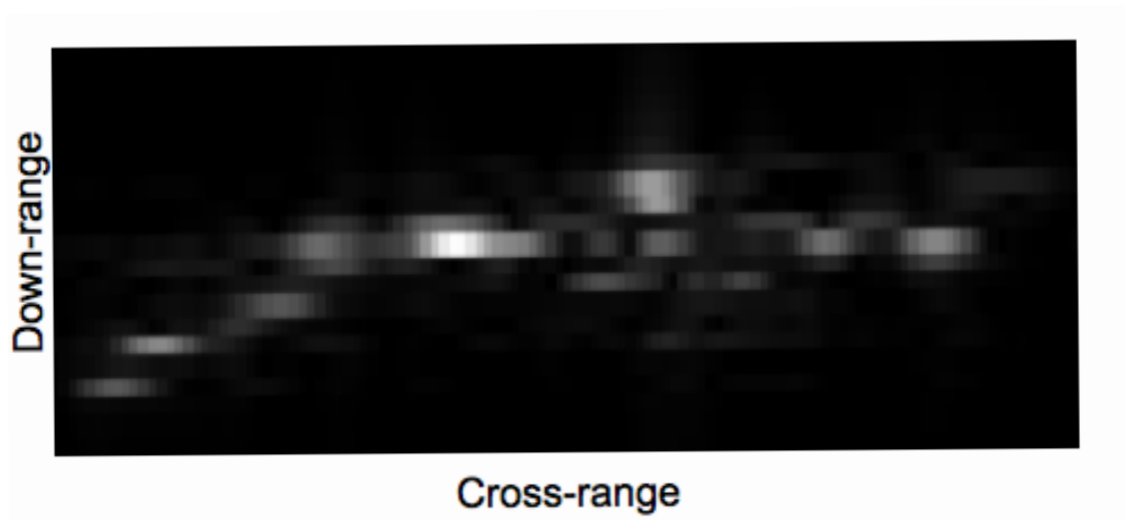


Figure 38. ISAR image using STFT with a hamming window, size 80 points and 50 percent of overlapping (Horizontal Polarization) - (1^{th} frame)

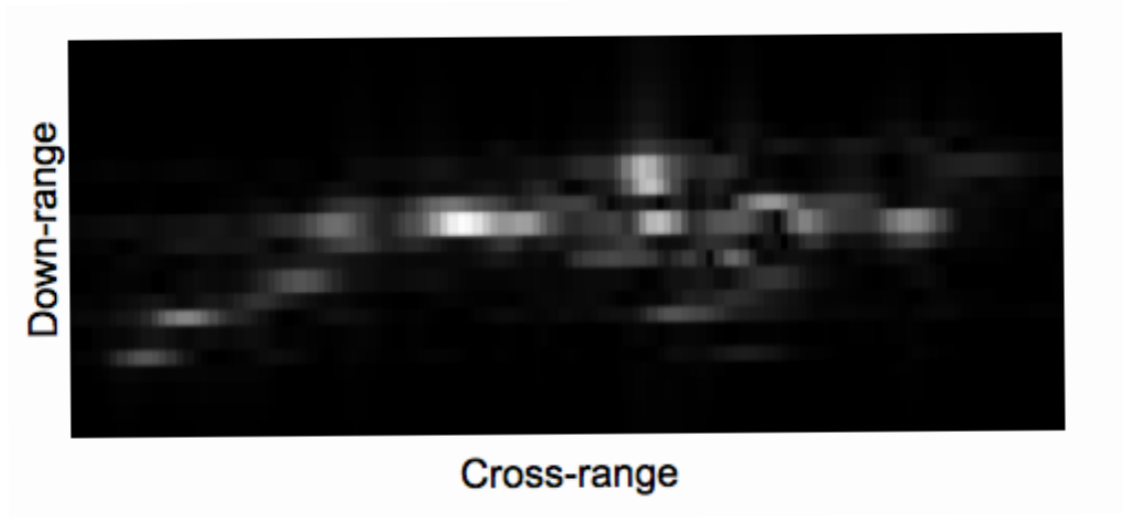


Figure 39. ISAR image using STFT with a hamming window, size 100 points and 50 percent of overlapping (Horizontal Polarization) - (1^{th} frame)

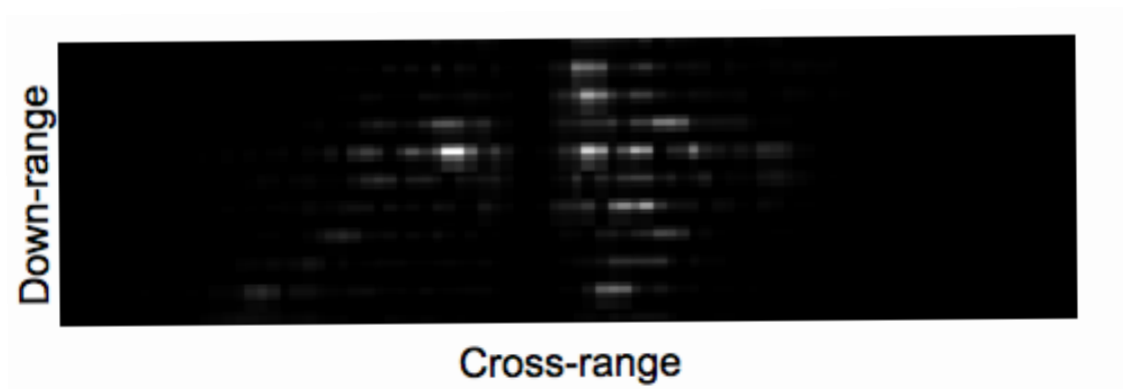


Figure 40. ISAR image using CWT with a mexican hat window, using a scale of 1:5 (Horizontal Polarization)

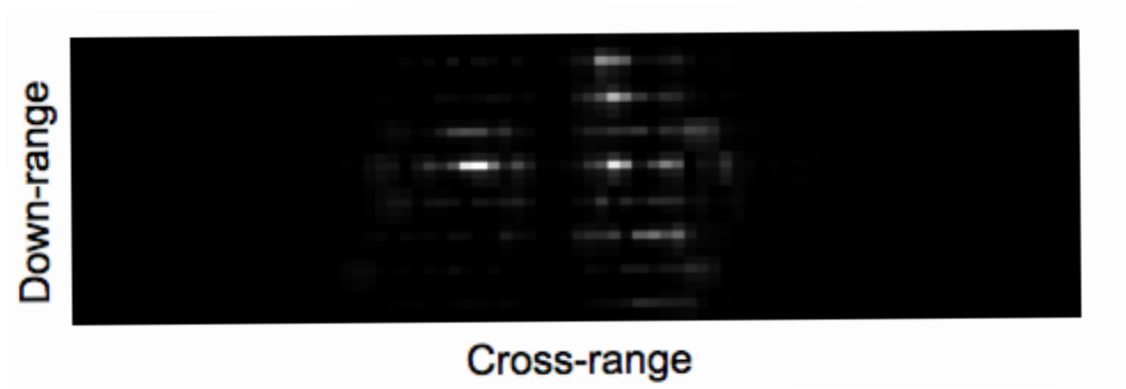


Figure 41. ISAR image using CWT with a mexican hat window, using a scale of 3:6 (Horizontal Polarization)

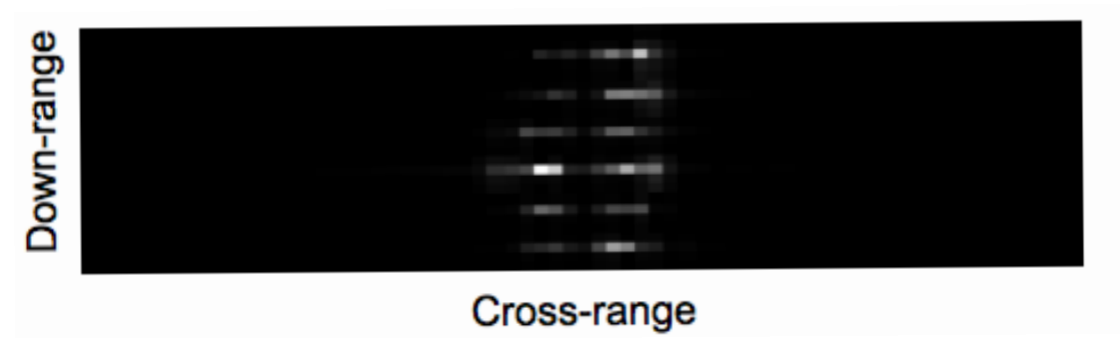


Figure 42. ISAR image using CWT with a mexican hat window, using a scale of 10:13 (Horizontal Polarization)

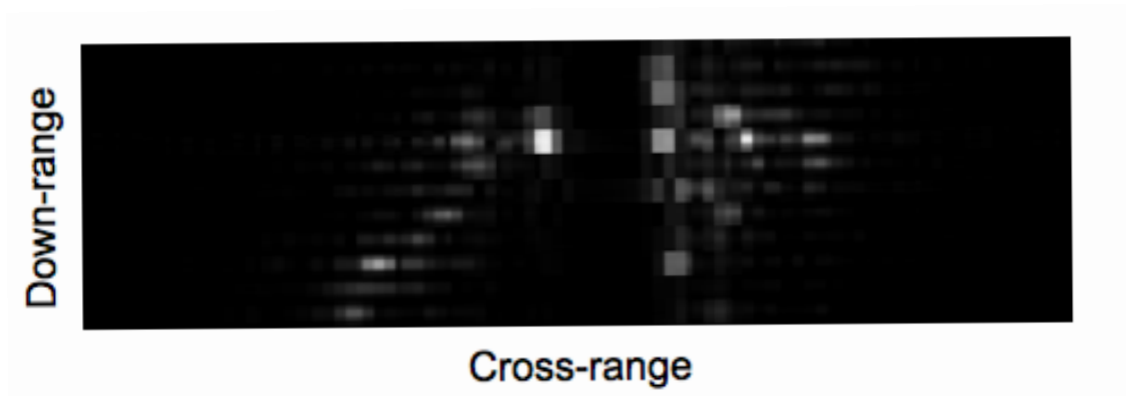


Figure 43. ISAR image using CWT with a Morlet window (Horizontal Polarization)

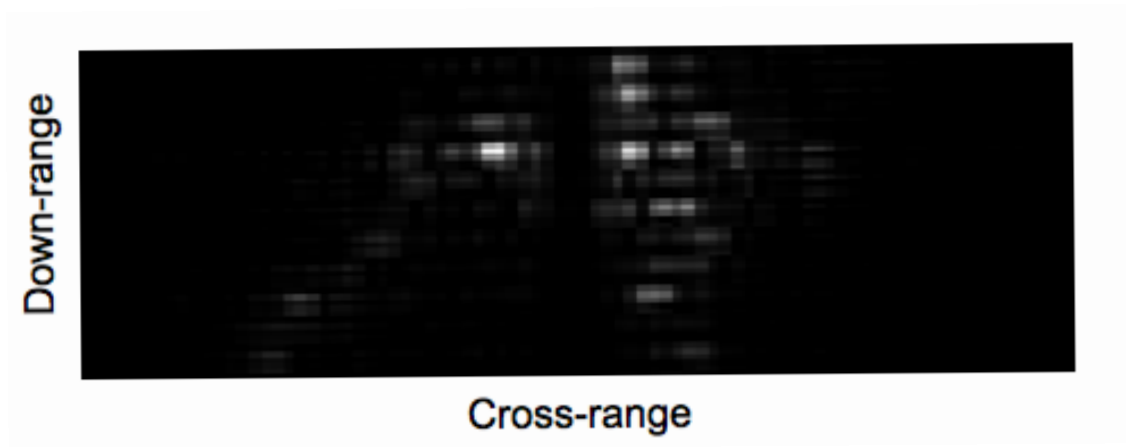


Figure 44. ISAR image using CWT with a Daubechies 2 window (Horizontal Polarization)

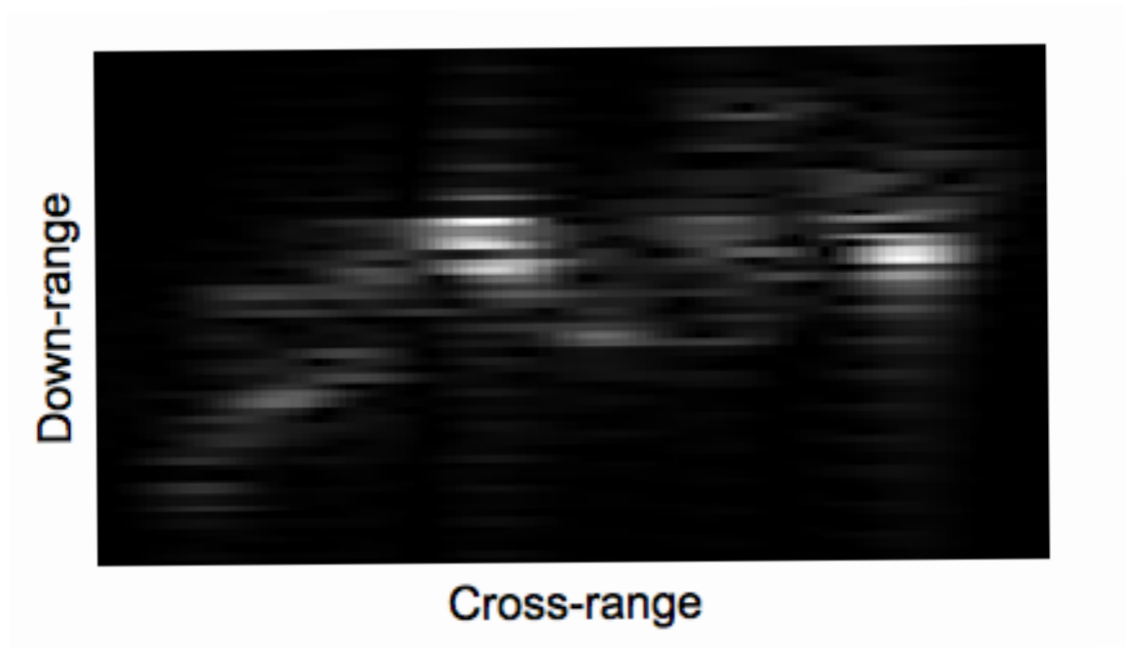


Figure 45. ISAR image using STFT with a hamming window, size 40 points and 50 percent of overlapping (Cross Polarization) - (3^{th} frame)

THIS PAGE INTENTIONALLY LEFT BLANK

VI. CONCLUSIONS

Production of ISAR images using time-frequencies methods instead of advanced algorithms for motion compensation has been analyzed in this thesis because of their potential for fast processing speeds. In military applications, time is always an important variable. There are some situations in which seconds could mean lives. The use of Fourier and wavelet transforms applied to ISAR imaging can be very important for identifying flying targets in a very fast way.

We compared the ISAR images produced using the STFT and the CWT. To accomplish this objective, complex backscatter data from a backhoe loader was used to exercise the algorithms.

The big problem with the Fourier approach is its limitation concerning the uncertainty principle: it's not possible to resolve both time and frequency with arbitrary accuracy. On the other hand, the window width can be adjusted for different frequencies in the CWT, so a good improvement in resolution can be obtained. With the ISAR imaging model, if the target drastically changes its flight path the image will always display some artifacts due to this change. In this situation, we observed that we can have some improvement using the CWT instead of the STFT. Because of its higher resolution for higher frequencies some of the artifacts are eliminated, a property that may allow us to increase the probability of identification (observe Figure 40 and Figure 37).

If a target presents a complex path, with fast maneuvers the images will always be displayed as blurred and with some extra scattering points due to aspect change of the target. But, using the CWT we can obtain better results and increase the quality of the image. In all the images we could observed that the CWT had superior resolution in the test cases. Since we can adjust the scale in the wavelet transform, we can always tune the scale to obtain better results in different flight paths, different speeds and different distances from the radar. We have more freedom in this method

than in the Fourier Transform approach. Thinking about the future, using some post processing technics we can improve the image. We can use noise filters, erosion technics and others. We should also exercise the algorithms with real data. Following that, improving the algorithms to be used receiving real time data from the radar. This will allow us to obtain different images each 2 to 3 sec and with this data we can better analyze and identify the target. This also allow us to reconstruct a movie from the data to see each aspect of the target during the time we were collecting the data.

APPENDIX A. MATLAB CODE FOR TEST CASE 1

```
clear all;
A95=getbackhoe(95,42);
A96=getbackhoe(96,42);
A97=getbackhoe(97,42);
A98=getbackhoe(98,42);
A99=getbackhoe(99,42);
A100=getbackhoe(100,42);
A101=getbackhoe(101,42);
A102=getbackhoe(102,42);
```

```
%elv=42.5; 94.5<Az>95.5
B95=A95.hh(:,1,:);
Xk=[];
MN95=[];
for i=1:14;
    f=170:214;
    Xk=B95(f,1,i);
    MN95=[MN95,Xk];
end
```

```
%elv=42.5; 95.5<Az>96.5
B96=A96.hh(:,1,:);
Xk=[];
MN96=[];
for i=1:14;
    f=170:214;
    Xk=B96(f,1,i);
    MN96=[MN96,Xk];
end
```

```
%elv=42.5; 96.5<Az>97.5
B97=A97.hh(:,1,:);
Xk=[];
MN97=[];
for i=1:14;
    f=170:214;
    Xk=B97(f,1,i);
    MN97=[MN97,Xk];
```


end

%elv=42.5; 97.5<Az>98.5

B98=A98.hh(:,1,:);

Xk=[];

MN98=[];

for i=1:14;

 f=170:214;

 Xk=B98(f,1,i);

 MN98=[MN98,Xk];

end

%elv=42.5; 98.5<Az>99.5

B99=A99.hh(:,1,:);

Xk=[];

MN99=[];

for i=1:14;

 f=170:214;

 Xk=B99(f,1,i);

 MN99=[MN99,Xk];

end

%elv=42.5; 99.5<Az>100.5

MN100=[];

Xk=[];

B100=A100.hh(:,1,:);

for i=1:14;

 f=170:214;

 Xk=B100(f,1,i);

 MN100=[MN100,Xk];

end

%elv=42.5; 100.5<Az>101.5

B101=A101.hh(:,1,:);

Xk=[];

MN101=[];

for i=1:14;

 f=170:214;

 Xk=B101(f,1,i);

 MN101=[MN101,Xk];

end

%elv=42.5; 101.5<Az>102.5

```

B102=A102.hh(:,1,:);
MN102=[];
Xk=[];
for i=1:14;
    f=170:214;
    Xk=B102(f,1,i);
    MN102=[MN102,Xk];
end

% Data Matrix formation
MN2 =[MN95, MN96, MN97, MN98, MN99, MN100, MN101, MN102];
% Display data matrix
% p2=abs(MN2);
% figure, imshow(p2,[]);
% xlabel('theta - 95 to 102, phi=42deg');
% ylabel('frequency (amplitude)');

% Range profiles calculation
DR=[];
for i=1:112;
    XR=fftshift(fft(MN2(:,i)));
    DR=[DR,XR];
end

%Display range profiles
% DRABS=abs(DR);
% figure, imshow(DRABS,[]);

% Apply Short-time Fourier transform to generate ISAR Image
Sf=[];
L=32;
noverlap=16;
for i=1:45;
    S=spectrogram(DR(i,:),hamming(80),40);
    Sf(:,:,i)=fftshift(S);
end

SFABS=abs(Sf);

%Display ISAR Image
Image = [SFABS(:,:,1) SFABS(:,:,2) SFABS(:,:,3) SFABS(:,:,4) SFABS(:,:,5)

```

```

SFABS(:,:,6) SFABS(:,:,7) SFABS(:,:,8) SFABS(:,:,9) SFABS(:,:,10)
SFABS(:,:,11) SFABS(:,:,12) SFABS(:,:,13) SFABS(:,:,14) SFABS(:,:,15)
SFABS(:,:,16) SFABS(:,:,17) SFABS(:,:,18) SFABS(:,:,19) SFABS(:,:,20)
SFABS(:,:,21) SFABS(:,:,22) SFABS(:,:,23) SFABS(:,:,24) SFABS(:,:,25)
SFABS(:,:,26) SFABS(:,:,27) SFABS(:,:,28) SFABS(:,:,29) SFABS(:,:,30)
SFABS(:,:,31) SFABS(:,:,32) SFABS(:,:,33) SFABS(:,:,34) SFABS(:,:,35)
SFABS(:,:,36) SFABS(:,:,37) SFABS(:,:,38) SFABS(:,:,39) SFABS(:,:,40)
SFABS(:,:,41) SFABS(:,:,42) SFABS(:,:,43) SFABS(:,:,44) SFABS(:,:,45)];
Imagew= Image/(max(max(Image)));
figure , imshow(Imagew,[0 1]);
%colormap(1-gray);
ylabel('Cross-range');
xlabel('Down-Range');

%Choosing frame to display
Image2=[];
for i=1:45;
    Imf=SFABS(:,1,i);
    Image2=[Image2,Imf];
end

%Display ISAR IMAGE
figure , imshow(Image2,[]);
ylabel('Cross-range');
xlabel('Down-range1');

%%%%%%%%%%%%%%%%%%%%%%%%%%%%%%%%%%%%%%%%%%%%%%%%%%%%%%%%%%%%%%%%%%%%%%%%%% Algorithm 2 %%%%%%%%%%%%%%%%%%%%%%%%%%%%%%%%%%%%%%%%%%%%%%%%%%%%%%%%%%%%%%%%%%%%%%%%%%%
clear all;
A95=getbackhoe(95,42);
A96=getbackhoe(96,42);
A97=getbackhoe(97,42);
A98=getbackhoe(98,42);
A99=getbackhoe(99,42);
A100=getbackhoe(100,42);
A101=getbackhoe(101,42);
A102=getbackhoe(102,42);

%elv=42.5; 94.5<Az>95.5
B95=A95.hh(:,1,:);
Xk=[];
MN95=[];
for i=1:14;

```

```

        f=170:214;
        Xk=B95(f,1,i);
        MN95=[MN95,Xk];
    end

    %elv=42.5; 95.5<Az>96.5
    B96=A96.hh(:,1,:);
    Xk=[];
    MN96=[];
    for i=1:14;
        f=170:214;
        Xk=B96(f,1,i);
        MN96=[MN96,Xk];
    end

    %elv=42.5; 96.5<Az>97.5
    B97=A97.hh(:,1,:);
    Xk=[];
    MN97=[];
    for i=1:14;
        f=170:214;
        Xk=B97(f,1,i);
        MN97=[MN97,Xk];
    end

    %elv=42.5; 97.5<Az>98.5
    B98=A98.hh(:,1,:);
    Xk=[];
    MN98=[];
    for i=1:14;
        f=170:214;
        Xk=B98(f,1,i);
        MN98=[MN98,Xk];
    end

    %elv=42.5; 98.5<Az>99.5
    B99=A99.hh(:,1,:);
    Xk=[];
    MN99=[];
    for i=1:14;
        f=170:214;
        Xk=B99(f,1,i);

```

```

        MN99=[MN99,Xk];
end

%elv=42.5; 99.5<Az>100.5
MN100=[];
Xk=[];
B100=A100.hh(:,1,:);
for i=1:14;
    f=170:214;
    Xk=B100(f,1,i);
    MN100=[MN100,Xk];
end

%elv=42.5; 100.5<Az>101.5
B101=A101.hh(:,1,:);
Xk=[];
MN101=[];
for i=1:14;
    f=170:214;
    Xk=B101(f,1,i);
    MN101=[MN101,Xk];
end

%elv=42.5; 101.5<Az>102.5
B102=A102.hh(:,1,:);
MN102=[];
Xk=[];
for i=1:14;
    f=170:214;
    Xk=B102(f,1,i);
    MN102=[MN102,Xk];
end

% Data MAtrix formation
MN2 =[MN95, MN96, MN97, MN98, MN99, MN100, MN101, MN102];
% Display data matrix
%p2=abs(MN2);
% figure, imshow(p2,[]);
% xlabel('theta - 95 to 102, phi=42deg');
% ylabel('frequency (amplitude)');

% Range profiles calculation

```

```

RP=[];
for i=1:112;
    XR=fftshift(fft2(MN2(:,i)));
    RP=[RP,XR];
end
%Padding array
RFP = padarray(RP,[8 8]);

% Apply Short-time Wavelet transform to generate ISAR Image
Sf=[];
F=[];
L=32;
noverlap=16;
cd=[];
for i = 1:61;
    %c = cwt(RFP(i,:),1:25,'sym4');
    % c = cwt(RFP(i,:),[3 18 12.9 7 1.5],'db2');
    % c = cwt(RFP(i,:),[16 8 6:-1:1],'morl'); %16 8 6
    c = cwt(RFP(i,:),1:5,'mexh'); %2:5
    Sf(:,:,i) =ifftshift(ifft2(c)); %coefficients
end

SFABS=abs(Sf);

%Display ISAR Image
Image = [SFABS(:,:,1); SFABS(:,:,2); SFABS(:,:,3); SFABS(:,:,4); SFABS(:,:,5);
SFABS(:,:,6); SFABS(:,:,7); SFABS(:,:,8); SFABS(:,:,9); SFABS(:,:,10);
SFABS(:,:,11); SFABS(:,:,12); SFABS(:,:,13); SFABS(:,:,14); SFABS(:,:,15);
SFABS(:,:,16); SFABS(:,:,17); SFABS(:,:,18); SFABS(:,:,19); SFABS(:,:,20);
SFABS(:,:,21); SFABS(:,:,22); SFABS(:,:,23); SFABS(:,:,24); SFABS(:,:,25);
SFABS(:,:,26); SFABS(:,:,27); SFABS(:,:,28); SFABS(:,:,29); SFABS(:,:,30);
SFABS(:,:,31); SFABS(:,:,32); SFABS(:,:,33); SFABS(:,:,34); SFABS(:,:,35);
SFABS(:,:,36); SFABS(:,:,37); SFABS(:,:,38); SFABS(:,:,39); SFABS(:,:,40);
SFABS(:,:,41); SFABS(:,:,42); SFABS(:,:,43); SFABS(:,:,44); SFABS(:,:,45)];

Imagew= Image/(max(max(Image)));
%Imag = imadjust(Imagew,[.07;.5],[0;1]);
%Imag = histeq(Imagew,64);
%Imag = adapthisteq(Imagew);
figure, imshow(Imagew,[]);
% colormap(1-gray);
ylabel('Range');

```

```

xlabel('Down-range');

%Choosing frame to display
Image2=[];
for i=1:45;
    Imf2=SFABS(2, :, i);
    Image2=[Image2; Imf2];
end

%Display ISAR IMAGE
figure , imshow(Image2, []);
ylabel('Cross-range');
xlabel('Down-range');

```

APPENDIX B. MATLAB CODE FOR TEST CASE 2

```
clear all;
% Extraction data from database
A95=getbackhoe(95,38);
A96=getbackhoe(96,38);
A97=getbackhoe(97,38);
A98=getbackhoe(98,38);
A99=getbackhoe(99,39);
A100=getbackhoe(99,40);
A101=getbackhoe(99,41);
A102=getbackhoe(99,42);
```

```
%elv=38.5; 94.5<Az>95.5
B95=A95.hh(:,1,:);
Xk=[];
MN95=[];
for i=1:14;
    f=170:214;
    Xk=B95(f,1,i);
    MN95=[MN95,Xk];
end
```

```
%elv=38.5; 95.5<Az>96.5
B96=A96.hh(:,1,:);
Xk=[];
MN96=[];
for i=1:14;
    f=170:214;
    Xk=B96(f,1,i);
    MN96=[MN96,Xk];
end
```

```
%elv=38.5; 96.5<Az>97.5
B97=A97.hh(:,1,:);
Xk=[];
MN97=[];
for i=1:14;
    f=170:214;
    Xk=B97(f,1,i);
```



```

        MN97=[MN97,Xk];
end

%elv=38.5; 97.5<Az>98.5
B98=A98.hh(:,1,:);
Xk=[];
MN98=[];
for i=1:14;
    f=170:214;
    Xk=B98(f,1,i);
    MN98=[MN98,Xk];
end

%38.5<elv>39.5; Az=99.5
B99=A99.hh(:, :, 7);
Xk=[];
MN99=[];
for i=1:14;
    f=170:214;
    Xk=B99(f,i,1);
    MN99=[MN99,Xk];
end

%39.5<elv>40.5; Az=99.5

MN100=[];
Xk=[];
B100=A100.hh(:, :, 7);
for i=1:14;
    f=170:214;
    Xk=B100(f,i,1);
    MN100=[MN100,Xk];
end

%40.5<elv>41.5; Az=99.5
B101=A101.hh(:, :, 7);
Xk=[];
MN101=[];
for i=1:14;
    f=170:214;
    Xk=B101(f,i,1);
    MN101=[MN101,Xk];

```

```

end

%41.5<elv>42.5; Az=99.5

B102=A102.hh(:, :, 7);
MN102=[];
Xk=[];
for i=1:14;
    f=170:214;
    Xk=B102(f,i,1);
    MN102=[MN102,Xk];
end

% Data Matrix formation
MN2 =[MN95, MN96, MN97, MN98, MN99, MN100, MN101, MN102];

%Plot data Matrix
p2=abs(MN2);
figure, imshow(p2, []);
xlabel('theta - 95 to 102, phi=42deg');
ylabel('frequency (amplitude)');

%Range profiles calculation
DR=[];
for i=1:112;
    XR=fftshift(fft(MN2(:,i)));
    DR=[DR,XR];
end

% Display Range-profiles
% DRABS=abs(DR);
% figure, imshow(DRABS, []);

% Apply Fourier tranform to all lines to form the ISAR image
Sf=[];
L=32;
noverlap=16;
for i=1:45;
    S=spectrogram(DR(i,:),hamming(100),50);
    Sf(:, :, i)=fftshift(S);
end
SFABS=abs(Sf);

```

```

Image = [SFABS(:,:,1) SFABS(:,:,2) SFABS(:,:,3) SFABS(:,:,4) SFABS(:,:,5)
SFABS(:,:,6) SFABS(:,:,7) SFABS(:,:,8) SFABS(:,:,9) SFABS(:,:,10)
SFABS(:,:,11) SFABS(:,:,12) SFABS(:,:,13) SFABS(:,:,14) SFABS(:,:,15)
SFABS(:,:,16) SFABS(:,:,17) SFABS(:,:,18) SFABS(:,:,19) SFABS(:,:,20)
SFABS(:,:,21) SFABS(:,:,22) SFABS(:,:,23) SFABS(:,:,24) SFABS(:,:,25)
SFABS(:,:,26) SFABS(:,:,27) SFABS(:,:,28) SFABS(:,:,29) SFABS(:,:,30)
SFABS(:,:,31) SFABS(:,:,32) SFABS(:,:,33) SFABS(:,:,34) SFABS(:,:,35)
SFABS(:,:,36) SFABS(:,:,37) SFABS(:,:,38) SFABS(:,:,39) SFABS(:,:,40)
SFABS(:,:,41) SFABS(:,:,42) SFABS(:,:,43) SFABS(:,:,44) SFABS(:,:,45)];
Imagew= Image/(max(max(Image)));
figure, imshow(Imagew,[0 1]);
ylabel('Cross Range');
xlabel('Range');

% Choose one frame to display
Image2=[];
for i=1:45;
Imf=SfABS(:,1,i);
Image2=[Image2,Imf];
end

% Display frame
figure, imshow(Image2,[]);
ylabel('Range');
xlabel('Cross Range');

%%%%%%%%%%%%%%%%%%%%%%%%%%%%%%%%%%%%%%%%%%%%%%%%%%%%%%%%%%%%%%%%%%%%%%%%%% Algorithm 2 %%%%%%%%%%%%%%%%%%%%%%%%%%%%%%%%%%%%%%%%%%%%%%%%%%%%%%%%%%%%%%%%%%%%%%%%%%%

clear all;
A95=getbackhoe(95,38);
A96=getbackhoe(96,38);
A97=getbackhoe(97,38);
A98=getbackhoe(98,38);
A99=getbackhoe(99,39);
A100=getbackhoe(99,40);
A101=getbackhoe(99,41);
A102=getbackhoe(99,42);

%elv=38.5; 94.5<Az>95.5
B95=A95.hh(:,1,:);

```

```

Xk=[];
MN95=[];
for i=1:14;
    f=170:214;
    Xk=B95(f,1,i);
    MN95=[MN95,Xk];
end

%elv=38.5; 95.5<Az>96.5
B96=A96.hh(:,1,:);
Xk=[];
MN96=[];
for i=1:14;
    f=170:214;
    Xk=B96(f,1,i);
    MN96=[MN96,Xk];
end

%elv=38.5; 96.5<Az>97.5
B97=A97.hh(:,1,:);
Xk=[];
MN97=[];
for i=1:14;
    f=170:214;
    Xk=B97(f,1,i);
    MN97=[MN97,Xk];
end

%elv=38.5; 97.5<Az>98.5
B98=A98.hh(:,1,:);
Xk=[];
MN98=[];
for i=1:14;
    f=170:214;
    Xk=B98(f,1,i);
    MN98=[MN98,Xk];
end

%38.5<elv>39.5; Az=99.5
B99=A99.hh(:, :, 7);
Xk=[];
MN99=[];

```

```

for i=1:14;
    f=170:214;
    Xk=B99(f,i,1);
    MN99=[MN99,Xk];
end

%39.5<elv>40.5; Az=99.5
MN100=[];
Xk=[];
B100=A100.hh(:,: ,7);
for i=1:14;
    f=170:214;
    Xk=B100(f,i,1);
    MN100=[MN100,Xk];
end

%40.5<elv>41.5; Az=99.5
B101=A101.hh(:,: ,7);
Xk=[];
MN101=[];
for i=1:14;
    f=170:214;
    Xk=B101(f,i,1);
    MN101=[MN101,Xk];
end

%41.5<elv>42.5; Az=99.5
B102=A102.hh(:,: ,7);
MN102=[];
Xk=[];
for i=1:14;
    f=170:214;
    Xk=B102(f,i,1);
    MN102=[MN102,Xk];
end

% Data Matrix formation
MN2 =[MN95, MN96, MN97, MN98, MN99, MN100, MN101, MN102];

%Display data matrix
p2=abs(MN2);
figure, imshow(p2,[]);

```

```

xlabel('theta - 95 to 102, phi=42deg');
ylabel('frequency (amplitude)');

%Range profiles calculation
RP=[];
for i=1:112;
    XR=fftshift(fft2(MN2(:,i)));
    RP=[RP,XR];
end

% Array Padding
RFP = padarray(RP,[8 8]);

%% Apply Wavelet tranform to all lines to form the ISAR image
Sf=[];
F=[];
L=32;
noverlap=16;
cd=[];
for i = 1:61;
%c = cwt(RFP(i,:),1:25,'sym4');
c = cwt(RFP(i,:),[3 18 12.9 7 1.5],'db2');
% c = cwt(RFP(i,:),[16 8 6:-1:1],'morl');
% c = cwt(RFP(i,:),10:13,'mexh');
Sf(:,:,i) =ifftshift(ifft2(c)); %coefficients
end

SFABS=abs(Sf);

%Display ISAR image
Image = [SFABS(:,:,1); SFABS(:,:,2); SFABS(:,:,3); SFABS(:,:,4); SFABS(:,:,5);
SFABS(:,:,6); SFABS(:,:,7); SFABS(:,:,8); SFABS(:,:,9); SFABS(:,:,10);
SFABS(:,:,11); SFABS(:,:,12); SFABS(:,:,13); SFABS(:,:,14); SFABS(:,:,15);
SFABS(:,:,16); SFABS(:,:,17); SFABS(:,:,18); SFABS(:,:,19); SFABS(:,:,20);
SFABS(:,:,21); SFABS(:,:,22); SFABS(:,:,23); SFABS(:,:,24); SFABS(:,:,25);
SFABS(:,:,26); SFABS(:,:,27); SFABS(:,:,28); SFABS(:,:,29); SFABS(:,:,30);
SFABS(:,:,31); SFABS(:,:,32); SFABS(:,:,33); SFABS(:,:,34); SFABS(:,:,35);
SFABS(:,:,36); SFABS(:,:,37); SFABS(:,:,38); SFABS(:,:,39); SFABS(:,:,40);
SFABS(:,:,41); SFABS(:,:,42); SFABS(:,:,43); SFABS(:,:,44); SFABS(:,:,45)];
Imagew= Image/(max(max(Image)));
figure, imshow(Imagew,[]);
ylabel('Range1');

```

```
xlabel('Doppler frequency');

%Display ISAR Image
Image2=[];
for i=1:45;
    Imf2=SFABS(1,:,i);
    Image2=[Image2;Imf2];
end
```

LIST OF REFERENCES

- [1] George Arfken. *Mathematical Methods for Physicists*, volume Third Edition. Harcourt Brace Jovanovich, 1985.
- [2] Ian G. Cumming and Frank H. Wong *Digital processing of Synthetic Aperture Radar Data*. Artech House Inc., 2005.
- [3] Mehrdad Soumekh *Synthetic Aperture Radar Signal Processing*. John Wiley and Sons Inc., 1999.
- [4] Victor C.Chen and Hao Ling. *Time-Frequency Transforms for Radar Imaging and Signal Analysis*. Artech House Inc., 2002.
- [5] Ronald N. Bracewell. *The Fourier Transform and its Applications*, volume Third Edition. McGraw-Hill Higher Education, 2000.
- [6] Dan E. Dudgeon and Russel M. Mersereau. *Multidimensional Digital Signal Processing*. Prentice-Hall Inc., 1984.
- [7] K.F.Riley, M.P. Hobson and S.J. Bence. *Matemtical Methods for Physics and Engineering* Cambridge University Press, 2006.
- [8] K.H. Wolfgang, Panofsky and Melba Phillips. *Classical Electrical and Magnetism*, volume Second Edition. Dover Publications Inc., 2005.
- [9] Brett Borden. *Radar Imaging of Airborne Targets: A Primer for Applied Mathematicians and Phycists* Institute of Physics Publishing Bristol and Philadelphia 1999.
- [10] Roberto Cristi. *Modern Digital Signal Processing*. Thomson, 2004.
- [11] Brett Borden. *Radar Class Notes*. April, 2007.
- [12] Yeungnam University. *Scattering mechanism and multi-aspects of radar signals*. <http://yu.ac.kr/kkt/research.html> (Last Accessed May 2007).
- [13] Pixon. *ISAR imaging using standartd Fourier Technic*. http://www.pixon.com/figures/FIG.ISAR_airplane.html (Last Accessed May 2007).
- [14] Sophocles J. Orfanidis. *Electromagnetic Waves and Antennas*. ECE Department Rutgers University. 94 Brett Road, Piscataway, NJ 08854-8058. orfanidi@ece.rutgers.edu. <http://www.ece.rutgers.edu/orfanidi/ewa/> (Last Accessed May 2007).

- [15] DSP guide. *Special Imaging Technics - Filtered Backprojection*.
<http://www.dspguide.com/ch25/5.htm> (Last Accessed Jun 2007).
- [16] A. W. Rihaczek, and S. J. Hershkowitz. *Radar Resolution and Complex - Image Analysis*. Artech House, 1996, ch.6.
- [17] David E. Newland. *Practical signal Analysis - Do Wavelets Mane Any Difference*. Proceedings, 1997.
- [18] Victor C. Chen and Shie Qian. *Joint Time-Frequency Transform for Radar Range-Doppler Imaging*. IEEE Transactions on Aerospace and Electronic Systems Vol.34, No.2, April 1995.
- [19] Oliver Rioul and Martin Vetterli. *Wavelets and Signal Processing Range-Doppler Imaging*. IEEE SP Magazine, October 1991.

INITIAL DISTRIBUTION LIST

1. Dudley Knox Library
Naval Postgraduate School
Monterey, CA
2. Professor Brett Borden
Naval Postgraduate School
Monterey, CA
3. Professor Roberto Cristi
Naval Postgraduate School
Monterey, CA
4. Chairman Physics Department
Naval Postgraduate School
Monterey, CA
5. Armando Jorge Lurecio
Directorate of Ships
Almada, Portugal